

AthenaK: A Performance-Portable Version of the Athena++ AMR Framework

JAMES M. STONE,^{1,2} PATRICK D. MULLEN,^{3,4} DRUMMOND FIELDING,^{5,6} PHILIPP GRETE,⁷ MINGHAO GUO,²
PHILIPP KEMPSKI,² ELIAS R. MOST,^{8,9} CHRISTOPHER J. WHITE,^{6,2} GEORGE N. WONG,^{1,10}

¹*School of Natural Sciences, Institute for Advanced Study, 1 Einstein Drive, Princeton, NJ 08540, USA*

²*Department of Astrophysical Sciences, Princeton University, Princeton, NJ 08544, USA*

³*CCS-2, Los Alamos National Laboratory, Los Alamos, NM*

⁴*Center for Theoretical Astrophysics, Los Alamos National Laboratory, Los Alamos, NM*

⁵*Department of Astronomy, Cornell University, Ithaca, NY 14853, USA*

⁶*Center for Computational Astrophysics, Flatiron Institute, 162 5th Avenue, New York, NY 10010, USA*

⁷*Hamburger Sternwarte, Universität Hamburg, Gojenbergsweg 112, 21029, Hamburg, Germany*

⁸*TAPIR, Mailcode 350-17, California Institute of Technology, Pasadena, CA 91125, USA*

⁹*Walter Burke Institute for Theoretical Physics, California Institute of Technology, Pasadena, CA 91125, USA*

¹⁰*Princeton Gravity Initiative, Princeton University, Princeton NJ 08544, USA*

Abstract

We describe **AthenaK**: a new implementation of the **Athena++** block-based adaptive mesh refinement (AMR) framework using the **Kokkos** programming model. Finite volume methods for Newtonian, special relativistic (SR), and general relativistic (GR) hydrodynamics and magnetohydrodynamics (MHD), and GR-radiation hydrodynamics and MHD, as well as a module for evolving Lagrangian tracer or charged test particles (e.g., cosmic rays) are implemented using the framework. In two companion papers we describe (1) a new solver for the Einstein equations based on the Z4c formalism and (2) a GRMHD solver in dynamical spacetimes also implemented using the framework, enabling new applications in numerical relativity. By adopting **Kokkos**, the code can be run on virtually any hardware, including CPUs, GPUs from multiple vendors, and emerging ARM processors. **AthenaK** shows excellent performance and weak scaling, achieving over one billion cell updates per second for hydrodynamics in three-dimensions on a single NVIDIA Grace Hopper processor and with a typical parallel efficiency of 80% on 65536 AMD GPUs on the OLCF Frontier system. Such performance portability enables **AthenaK** to leverage modern exascale computing systems for challenging applications in astrophysical fluid dynamics, numerical relativity, and multimessenger astrophysics.

Keywords: Astronomy software (1855), Computational methods (1965), Magnetohydrodynamics (1964), Hydrodynamics (1963)

1. INTRODUCTION

Given the critical role that numerical methods play in theoretical astrophysics, it is important that software that implements such methods be able to exploit the most capable high-performance computing (HPC) systems available. In recent years, however, HPC systems have become increasingly heterogeneous, incorporating novel architectures such as ARM processors or external accelerators such as graphical processing units (GPUs). Programming such systems often re-

quires adopting vendor-specific language extensions such as CUDA (from NVIDIA), HIP (from AMD), or SYCL (from Intel) or relying on the vendor to support open source standards such as OpenACC or OpenMP. Developing and maintaining software that runs effectively across diverse platforms is a challenge.

This issue is not confined to astrophysics, and fortunately generic solutions are emerging from the scientific computing community at large. For example, the **Kokkos**¹ programming model (Trott et al. 2022) is one such solution. It consists of C++ templates and abstrac-

tions that can be used to manage execution on heterogeneous systems with multiple memory spaces, execution spaces, and execution policies (e.g., scalar, vector, or shared-memory parallelism). When building software written with `Kokkos` for a particular HPC system, instructions are effectively translated into the native programming environment of the target architecture, enabling vendor optimizations that can improve performance. Thus, software developed with `Kokkos` becomes *performance-portable*.

This paper describes `AthenaK`: a completely new implementation of the adaptive mesh refinement (AMR) framework, fluid dynamics solvers, and general relativistic radiation transport solver in the `Athena++` code (Stone et al. 2020, hereafter S20) using the `Kokkos` programming model. In `AthenaK` the AMR and mesh are abstracted from the physics so that they can be used to solve a diverse range of problems. In two companion papers we describe a new solver for the Einstein equations of general relativity based on the Z4c formalism that has been implemented using the `AthenaK` AMR framework (Zhu et al. 2024), as well as a new GRMHD solver that works in dynamical spacetimes (Fields et al. 2024). We show that the AMR framework and solvers in `AthenaK` achieve excellent performance and parallel scaling across a wide range of architectures, including both CPUs and GPUs from a variety of vendors. Taken together these solvers enable problems in astrophysical fluid dynamics, numerical relativity, and multimessenger astrophysics to be tackled using modern exascale HPC systems.

`AthenaK` is not the first nor the only astrophysical fluids code that adopts `Kokkos`. In fact, Grete et al. (2021) have already described an implementation of the MHD solvers in `Athena++` on a uniform mesh using `Kokkos`. Subsequently the block-based AMR framework in `Athena++` has also been independently implemented in the `Parthenon` framework (Grete et al. 2023), and the latter now serves as the foundation for an increasing number of astrophysical application codes including `AthenaPK`², `KHARMA` (described in Prather 2024), and `Phoebus` (Rodriguez-Bueno et al. 2023). Recently, Lesur et al. (2023) have developed `IDEFIX`, a new implementation of the `PLUTO` code (Mignone et al. 2012) in `Kokkos`.

The `AthenaK` code is in fact an outgrowth of the `Parthenon` collaboration, and it shares many features in common both with the `Parthenon` framework and downstream codes such as `AthenaPK`, although there are also important differences. `Parthenon` is a much more ambitious, complex, and capable framework that has many

extensions that will make it useful for a wide variety of applications across many different disciplines. The `AthenaK` code described in this paper is a much smaller and simpler project, focused on applications in astrophysical fluid dynamics.

There are a variety of other astrophysical fluid codes that run on GPU-accelerated hardware by adopting vendor-specific tools such as CUDA. These include an implementation of the `RAMSES` code in CUDA (Kestener 2017), `Cholla` (Schneider & Robertson 2015) and more recently `Cholla-MHD` (Caddy & Schneider 2024), `H-AMR` (Liska et al. 2022), and `GAMER-2` (Schive et al. 2018). Other block-structured AMR packages that are GPU-enabled include `AMReX` (Zhang et al. 2019).

The `AthenaK` code described in this paper should be thought of as complementary to these other codes. What distinguishes it is the combination of (1) performance portability through `Kokkos`, (2) full block-structured AMR framework, (3) a wide variety of physics solvers, and (4) open source development which builds on previous versions of `Athena` (Stone et al. 2008, hereafter S08). Users of previous versions of `Athena` should be able to adopt their applications to `AthenaK` very easily.

In the following section, we describe the modifications necessary to implement the `Athena++` AMR framework in `AthenaK` using `Kokkos`. In §3 we describe the various fluid dynamic and GR-radiation transport solvers implemented in `AthenaK`, while in §4 we describe a particle module that includes methods for both plasma kinetics and Lagrangian tracer particles. In §5 we provide performance and scaling data on various architectures for the fluid solvers that demonstrate true performance portability. Finally, in §6 we conclude.

2. AMR FRAMEWORK

There are several inherent complexities associated with programming heterogeneous computing systems. Firstly, data may be stored in multiple memory spaces (e.g., on the host, on the device, or in a shared location), and the programmer is responsible for deciding what goes where. Similarly there may be multiple execution spaces (e.g., CPUs on a host as well as external accelerators such as GPUs), and again the programmer must control what is computed where. Finally, each different execution space may have a different architectures, i.e. scalar, vector, or shared-memory parallel processors, and the programmer must be able to control the execution strategy in each space individually.

Given these complexities, we found it easier to rewrite the `Athena++` AMR framework from scratch rather than trying to port it to `AthenaK`. In the end, very little of the

² <https://github.com/parthenon-hpc-lab/athenapk>

overall design was changed. Thus, Athena_K adopts the same block-based AMR design as in Athena++ with communication between levels occurring only at boundaries, flux corrections at level boundaries to enforce conservation, uniform time stepping across levels, and dynamical execution via a task list. Section 2 of S20 continues to serve as the primary reference for this framework; in the paragraphs below we only describe the extensions and modifications required for good performance across different architectures. We note that many of these ideas originate from the Parthenon collaboration, and therefore replicate features of that framework (Grete et al. 2023).

MeshBlockPacks: As in Athena++, in Athena_K the mesh is divided into structures termed MeshBlocks which are organized into a binary tree (octree in three dimensions) and labeled via Z-ordering. However, in Athena_K we have found it important to organize all MeshBlocks on the same device into an aggregate data structure called a MeshBlockPack. Since the operations in all MeshBlocks on the same device can be performed in parallel, this reduces the number of kernel launches and greatly enhances performance when there are a large number of small MeshBlocks on the same device.

Physics modules: Each physics module is stored as a C++ object in each MeshBlockPack. Each module is independent with its own memory and task list. This reduces the combinatorial complexity of building task lists, and enables multiple physics objects to be constructed simultaneously for calculations involving multiple fluids or numerical relativity with fluid dynamics.

Data locality: Dependent variables within each physics module are stored as $(N+1)$ -dimensional Kokkos Views, with the extra dimension being the index of the MeshBlock associated with the data. This data is always stored on the device, and is never moved to the host except for outputs. Conversely, the mesh binary tree is created, stored, and refined (with AMR) on the host. Any mesh data that needs to be accessed on both the host and device are stored as Kokkos DualViews. Fortunately the syntax of Views is nearly identical to the multidimensional array class in Athena++, making the transition seamless.

Execution spaces: Operations on dependent variables are always performed on the device, with the host controlling the creation and manipulation of the tree, and managing dynamic execution via the task list. To the extent possible, the default memory and execution spaces for any computationally intensive operations in Athena_K are always on the device.

Boundary conditions: As in both Athena and Athena++, boundary conditions for the dependent vari-

ables on each MeshBlock are applied via ghost zones. Communication of data between MeshBlocks to load the ghost cells is done within parallel kernels on the device, either as simple memory copies or to load data into a boundary buffer (allocated in device memory) that is then communicated via point-to-point MPI calls. The number of MPI messages sent between ranks is proportional to the number of MeshBlocks stored within the MeshBlockPack on each rank. When communicating data between different levels in an AMR grid, prolongation and restriction operations are also performed all at once inside parallel kernels. The boundary communication infrastructure in Athena_K has been largely redesigned from the original version in Athena++ to make it simpler and more flexible on shared-memory parallel devices.

Cartesian coordinates only: Currently, Athena_K only supports uniform Cartesian coordinates for a number of reasons. Firstly, applications with Athena_K target exascale HPC systems that enable very large calculations, and such calculations are generally best discretized with Cartesian coordinates. Moreover the difference between calculations performed in different coordinates is only at the level of truncation error, which should be small for any resolved calculation. In fact higher-order spatial discretizations are simpler in Cartesian coordinates, which can make them more accurate than curvilinear coordinates. Finally many elements of object-orientated programming such as virtual functions and polymorphism are not supported by the compilers currently available on many GPUs, and this means implementing different coordinates using the design in Athena++ would require significant changes. The primary limitation of not supporting curvilinear coordinates is that 2D axisymmetric calculations are not possible with Athena_K. Any applications that truly require curvilinear coordinates can always adopt Athena++ or other codes.

Generalized task list: The design of the task list in Athena_K has been improved to support more general operations. Separate task lists are built for multi-stage time integrators, operator split source terms, and multiple physics modules and then chained together, or interleaved as necessary. Which physics is included in a calculation is controlled simply by which set of tasks (and task lists) are executed at run time.

I/O: Data required for output is generally stored on the device, and so must first be copied to the host for output. However, this enables asynchronous outputs since the device can modify its own data while the host continues to write output. Parallel files are written using MPI-IO to a custom binary format with no dependence

on external libraries. Python scripts are provided that can translate AthenaK binary files to other formats, such as HDF5.

Building and compiling: AthenaK adopts `cmake` to control building the code for different architectures, largely because `Kokkos` supports external builds using this tool. This allows the numerous features of `Kokkos` to be controlled from command-line options during the build step. The physics and algorithm options in AthenaK are no longer controlled by a configure script as in Athena++. Instead, the entire source code is compiled and options are selected at run time using parameters in the input file, including a large number of problem generators (i.e., the functions that generate the initial conditions for a wide range of problems). This greatly simplifies testing and development. User-defined problem generators are easily included as a `cmake` command line option. Since the number of registers is extremely limited on many GPUs, we have found that the use of templating for some algorithmic options (e.g., Riemann solvers) reduces register spillage and can greatly improve performance.

Supporting open source development: The entire AthenaK source code is available in an public repository³, there are no private development versions. The code continues to be licensed under the permissive BSD-3 open source license. Contributions and feedback from the community are encouraged.

3. FLUID SOLVERS

Numerical methods for Newtonian, special relativistic (SR), and general relativistic (GR) hydrodynamics and MHD, and GR-radiation hydrodynamics and MHD, have all been implemented in AthenaK. In this section we describe each of these solvers, while in §5 we provide performance metrics on various devices.

The fluid solvers all integrate the coupled system of conservation laws

$$\frac{\partial \mathbf{U}}{\partial t} + \nabla \cdot \mathbf{F}(\mathbf{W}) = \mathbf{S} \quad (1)$$

where \mathbf{U} and \mathbf{F} are vectors of the conserved variables and their fluxes respectively, while \mathbf{W} is a vector of primitive variables and \mathbf{S} are source terms (if required). In general, an equation of state which relates the various thermodynamic variables must be specified to close the system.

For MHD, the induction equation for the evolution of the magnetic field \mathbf{B} must be evolved

$$\frac{\partial \mathbf{B}}{\partial t} + \nabla \times \mathbf{E} = 0 \quad (2)$$

where \mathbf{E} is the electric field which in general includes both inductive and non-ideal terms.

The numerical algorithms adopted by the fluid solvers are all based on higher-order finite-volume schemes. These schemes adopt a reconstruct, solve, and advance strategy. The details of the methods and their implementation in the Athena codes have already been published in a series of papers (Gardiner & Stone 2005, 2008; Stone et al. 2008; Beckwith & Stone 2011; White et al. 2016; Stone et al. 2020; White et al. 2023) and will not be repeated here, instead only general features of the implementation that are unique to AthenaK will be described.

For spatial reconstruction schemes, the piecewise linear method (PLM), two versions of the piecewise parabolic method using either the original (Colella & Woodward 1984, hereafter PPM4) or extremum-preserving limiters (McCorquodale et al. 2015, hereafter PPMX), and the improved WENOZ scheme of Acker et al. (2016) are implemented. These are selected by a parameter in the input file. Reconstruction is always performed on the primitive variables. As shown in S08, it is often advantageous to reconstruct the characteristic variables, however this option has not yet been implemented in AthenaK.

To compute fluxes of the conserved variables at cell interfaces, a variety of different Riemann solvers (Toro 2013) are implemented depending on the physics, including the local Lax-Friedrichs (LLF) method, various versions of the Harten-Lax-van Leer method including HLLE, HLLC, and HLLD, as well as Roe’s linearized solver.

To time-advance the solution, the method-of-lines approach is adopted. A variety of low storage, high-order strong-stability-preserving (SSP) Runge-Kutta (RK) integration schemes (Ketcheson 2010) are implemented in AthenaK, from RK1 through RK4. Explicit time integration requires the time step satisfy the constraint

$$\Delta t \leq \text{CFL} \cdot \min [(\Delta x_i)/\lambda_{\max,i}] \quad (3)$$

where $\lambda_{\max,i}$ is the maximum cell-centered signal speed in the i -th dimension in each cell, and the minimum is taken over all cells and all dimensions. The factor $\text{CFL} \leq 1$ depends on the specific time integrator and the dimensions N_{dim} of the problem. Generally we use $\text{CFL} \leq 1/N_{\text{dim}}$. Note that the Athena code also used the dimensionally-unsplit CTU algorithm of Colella (1990), which has many advantages for non-relativistic problems. However, since it does not extend easily to the relativistic equations of motion, a CTU integrator has not been implemented in AthenaK.

³ <https://github.com/IAS-Astrophysics/athenak>

For some problems which include very stiff source terms, implicit-explicit (IMEX) RK integrators have proved to be useful (Ascher et al. 1997). However, as shown by Krapp et al. (2024), many commonly used IMEX integrators fail to guarantee positivity of the solution, which is very problematic when stiff source terms are included in the energy equation. In Athena_K we have implemented several different IMEX integrators, and we describe their application to two-fluid MHD in §3.3.

For MHD, the magnetic field is discretized as area-averages on cell-faces, and the constrained transport (CT) algorithm of Evans & Hawley (1988) is used to preserve the divergence-free constraint with upwinded electric fields calculated using the method of Gardiner & Stone (2005, 2008). As discussed in S20, using face-centered fields complicates communication of ghost zones and flux conservation in the AMR framework, however we have found the use of the staggered mesh version of CT is critical for some problems.

Guaranteeing positivity of the density and internal energy in multidimensional higher-order finite-volume schemes is challenging in regions where the kinetic or magnetic energy is very large. This is not due to round-off error associated with differencing large numbers, but rather truncation error inherent to the scheme can become comparable to the magnitude of derived quantities such as pressure. To overcome this issue, in Athena_K we have implemented the first-order flux-correction (FOFC) scheme used in Lemaster & Stone (2009). In each stage of the SSP-RK integrators, if the density or pressure in any cell were to go negative, the fluxes on all faces of that cell are recalculated using first-order (piecewise constant) reconstruction and a diffusive LLF Riemann solver. This must be performed before flux corrections associated with level boundaries are made when using AMR. In practice, FOFC is applied extremely rarely (once in every $\sim 10^{10}$ cell updates in the supersonic turbulence application presented in Lemaster & Stone 2009). Nevertheless we find using FOFC greatly improves the stability of calculations in extreme regimes, for example it significantly reduces the need for floors in general relativistic MHD simulations of black hole accretion flows (see §3.5 and §3.6).

3.1. Non-relativistic Hydrodynamics

In Newtonian hydrodynamics the conserved variables and their fluxes are

$$\mathbf{U} = \begin{bmatrix} \rho \\ \rho \mathbf{v} \\ E \end{bmatrix}, \quad \mathbf{F} = \begin{bmatrix} \rho \mathbf{v} \\ \rho \mathbf{v} \mathbf{v} + p_g \\ (E + p_g) \mathbf{v} \end{bmatrix}, \quad (4)$$

where ρ is the mass density, \mathbf{v} the fluid velocity, p_g the gas pressure, $E = u_g + \rho v^2/2$ the gas total energy, and u_g the gas internal energy. The vector of primitive variables is $\mathbf{W} = [\rho, \mathbf{v}, u_g]$. An equation of state (EOS) $p_g = p_g(\rho, u_g)$ is required to close the system. For non-relativistic hydrodynamics in Athena_K, both a γ -law EOS $p_g = (\gamma - 1)u_g$ and an isothermal EOS $p_g = C^2 \rho$ are implemented, where γ is the ratio of specific heats and C the isothermal sound speed respectively. In the latter case the energy equation in (1) is not needed.

The accuracy and fidelity of the various reconstruction schemes, Riemann solvers, and time-integration algorithms implemented in Athena_K have been documented in many other references (e.g. S20, Toro 2013). Here, to demonstrate their implementation in Athena_K, we only present results from two simple test problems. Both are run on a single CPU core.

The first, and most quantitative, is to measure the convergence of errors in the propagation of linear waves. The left panel of Figure 1 shows the convergence of the L_1 error for both sound and entropy waves in one-dimensional hydrodynamics using various algorithmic options. Following S20, the problem is initialized using an exact eigenmode for each wave family and evolved for one wave period with a variety of spatial resolutions. In one-dimension, fourth-order convergence is observed for the extremum-preserving reconstruction schemes PPMX and WENOZ until either non-linear effects or round-off error becomes important, while both PPM with more aggressive limiters and PLM show second-order convergence.

The second test is the Shu-Osher shocktube (Shu & Osher 1989) which involves the interaction of a discontinuity with a smoothly varying background, and therefore demonstrates both the shock-capturing and diffusive properties of different methods. The right panel of Figure 1 shows the density at $t = 0.047$ when run with both PLM+RK2 and WENOZ+RK3 with 200 uniform grid cells. Clearly the extremum-preserving higher-order WENOZ method captures small scales in the problem more accurately than PLM.

Finally, to showcase how Athena_K can enable new applications at scale, we show preliminary results from a challenging calculation involving the interaction of a supernova blast wave with a turbulent, multiphase medium. Both heating and cooling source terms representative of physical processes in the ISM (Schneider & Robertson 2018) are included in the energy equation. The calculation begins with an initially uniform thermally unstable background in a cubic domain of size 32^3 pc on a grid of 2048^3 cells to which small perturbations are added. The system is evolved until the ther-

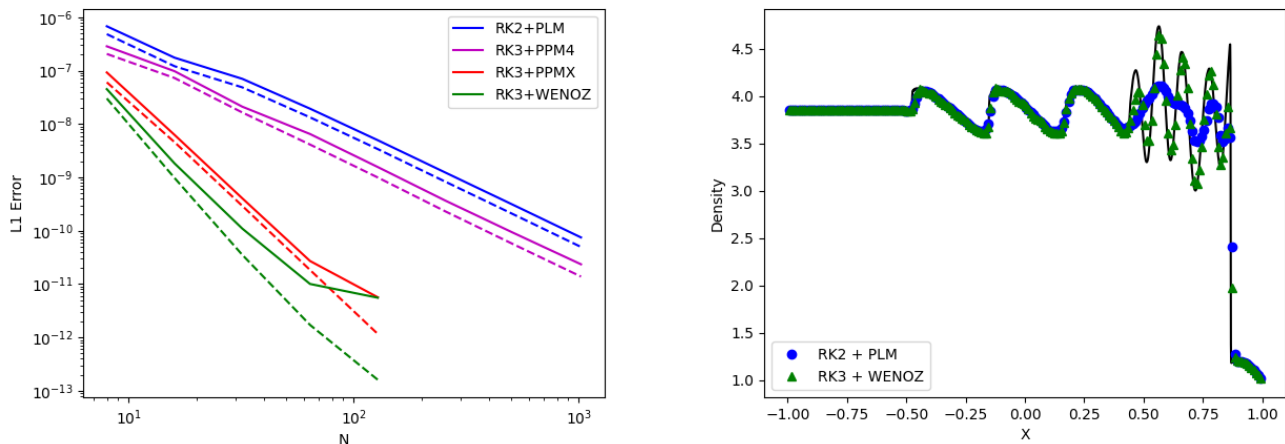


Figure 1. (Left) Linear wave convergence rates in 1D for both entropy (solid-line) and sound (dashed-line) waves for different methods. (Right) Density in the Shu-Osher shocktube test using 200 uniform cells and different methods. The solid black line is a reference solution computed using 2000 cells and RK3+WENOZ.

mal instability has gone nonlinear, generating a turbulent multiphase medium, at which point a spherical blast wave is initialized in the center of the domain by adding a region of high pressure. As this blast wave propagates through the background, it encounters dense cold filaments and clumps which produce further turbulence and mixing. The simulation uses an RK3+PPM4 integrator, the HLLC Riemann solver, and FOFC. Figure 2 shows a slice of the temperature at late time. Insets in the figure show specific regions of interest where nonlinear thin-shell instability, turbulent mixing, and shock-cloud interaction are occurring. The full calculation took only 2.4×10^3 GPU hours. A full analysis of the results, including how the time evolution of the shock wave is affected by mass entrainment and mixing is given in Guo (2024).

3.2. Non-relativistic MHD

In Newtonian MHD the conserved variables and their fluxes are

$$\mathbf{U} = \begin{bmatrix} \rho \\ \rho \mathbf{v} \\ E \end{bmatrix}, \quad \mathbf{F} = \begin{bmatrix} \rho \mathbf{v} \\ \rho \mathbf{v} \mathbf{v} - \mathbf{B} \mathbf{B} + p^* \\ (E + p^*) \mathbf{v} - \mathbf{B} (\mathbf{B} \cdot \mathbf{v}) \end{bmatrix}, \quad (5)$$

where $p^* = p_g + p_m$ is the sum of gas and magnetic pressures. For non-relativistic MHD, both a γ -law EOS (with $E = p_g/(\gamma - 1) + \rho v^2/2 + B^2/2$) and an isothermal gas EOS (with $p_g = C^2 \rho$) are implemented.

The left panel of Figure 3 shows the results for a one-dimensional linear wave convergence test for each MHD wave family using various algorithmic options run on a single CPU core. While fourth-order convergence is observed for RK3+PPMX and RK3+WENOZ for slow and

Alfvén waves, the fast wave only converges at second-order even in one-dimension. For PPM4 and PLM reconstruction, all waves converge at second-order, as expected.

The right panel of Figure 3 shows the density in the Brio-Wu shocktube (Brio & Wu 1988) using different methods run on a CPU. Since the solution mostly involves discontinuities, both methods perform similarly. Note the small amplitude ringing near the compound wave at $x = 0$. This can be significantly reduced by reconstructing characteristic variables instead of primitive variables (S20), although this option (which is complex in SR and GR) has not been implemented in AthenaK.

Finally, Figure 4 shows a simulation modeling isothermal, driven MHD turbulence on a 4096^3 grid including explicit viscosity and resistivity (see §3.3) at a Reynolds number of 2×10^5 and a magnetic Prandtl number of 1. The simulation uses WENOZ for spatial reconstruction, RK2 for time integration, an HLLD Riemann solver, and was run on 4096 GPUs on OLCF’s Frontier using 256^3 MeshBlocks. Turbulence is driven only on large scales, with an acceleration field following a parabolic power spectrum between $1 \leq 2\pi k/L_{\text{box}} \leq 3$, peaking at $2\pi k = 2L_{\text{box}}$. The driving is applied in real space rather than Fourier space to avoid the costly global communications required for FFTs in large domains. The turbulence driving field is restricted to be purely solenoidal (i.e., the driving field is divergence-free). The turbulent energy injection rate is set so that the root-mean-squared velocity is half of the sound speed, yielding $\mathcal{M} = v_{\text{rms}}/c_s = 0.5$. The mean magnetic flux in the domain corresponds to an Alfvén Mach number of 2. After several eddy turnover times, the tangled mag-

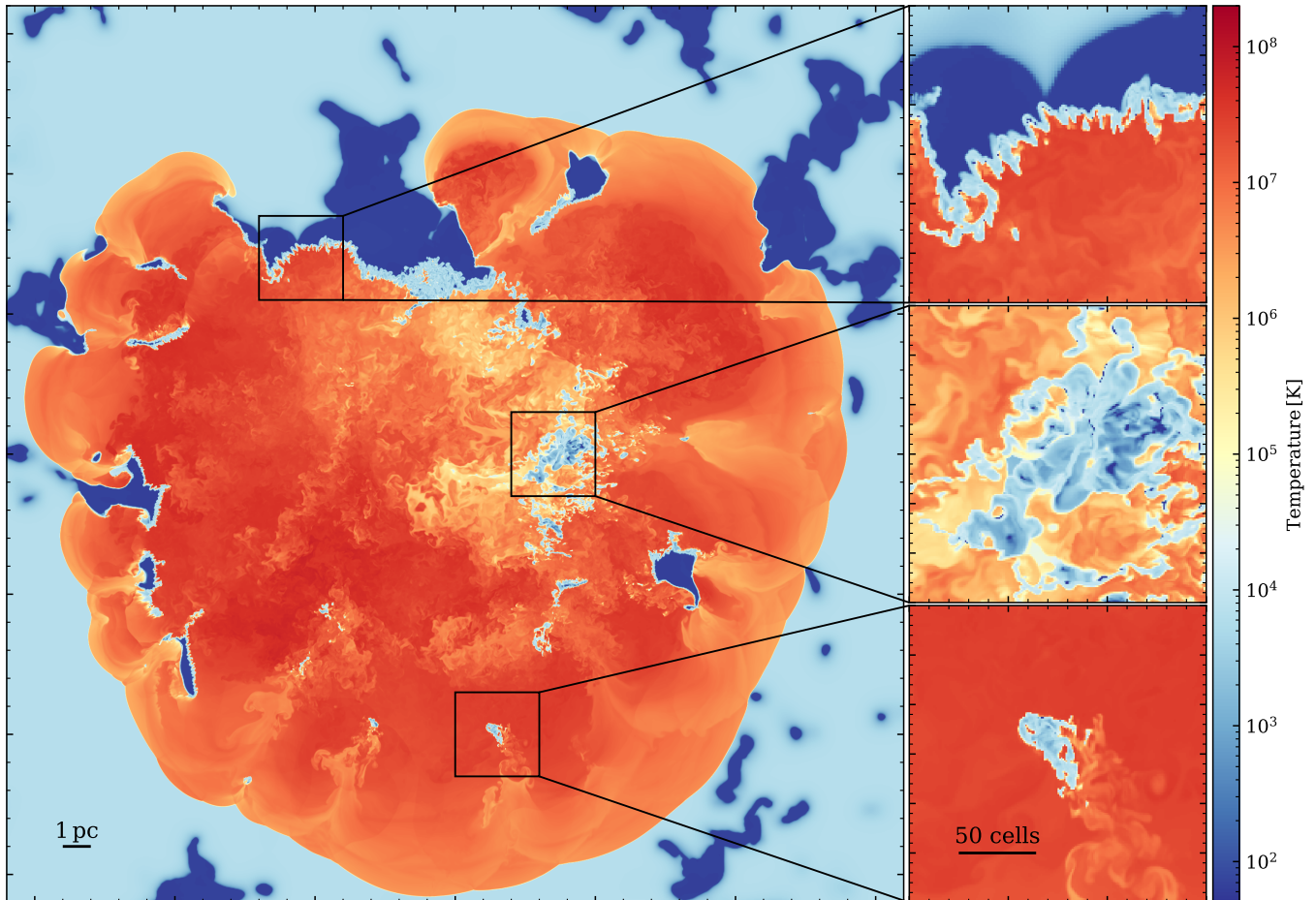


Figure 2. Slice of temperature through the $z = 0$ plane at time $t = 10$ kyr in a 3D simulation of a supernova blast wave interacting with a turbulent multiphase medium on a 2048^3 grid. Zoom-ins of selected regions in left panels show nonlinear thin-shell instability (top), turbulent mixing (middle), and single shock-cloud interaction (bottom).

netic field component dominates over the mean field, reaching a saturation ratio of approximately $\delta B/\bar{B} \approx 3$. The simulation was run for 4 eddy turnover times. The plot shows the magnitude of the current normalized by the grid spacing in a 2D slice through the 3D domain. The zoomed-in panels highlight the intricate small-scale structures typical of high-amplitude MHD turbulence.

3.3. Diffusion

Diffusive processes such as viscosity and thermal conduction can be included in non-relativistic problems through the addition of the appropriate fluxes to \mathbf{F} in Equation (1)

$$\mathbf{F}_{\text{visc}} = [0, \mathbf{\Pi}, (\mathbf{v} \cdot \mathbf{\Pi})], \quad (6)$$

$$\mathbf{F}_{\text{cond}} = [0, 0, \kappa \nabla T], \quad (7)$$

where $\mathbf{\Pi}$ is the viscous stress tensor (see Equation 7 in S20). Ohmic resistivity contributes to the flux

$$\mathbf{F}_{\text{Ohm}} = [0, 0, \eta \mathbf{J} \times \mathbf{B}] \quad (8)$$

and supplements the electric field \mathbf{E} in Equation (2) with a non-ideal term

$$\mathbf{E}_{\text{Ohm}} = \eta \mathbf{J}, \quad (9)$$

where $\mathbf{J} = (\nabla \times \mathbf{B})$ is the current density. When added in this fashion, the diffusive fluxes are computed explicitly at every stage of the RK time integrators rather than using operator splitting.

Adding diffusive terms to the evolution equations (1) makes them of mixed hyperbolic-parabolic form; explicit time integrators are thereby subject to a much more restrictive stability limit,

$$\Delta t \leq \text{CFL}_{\text{diff}} \cdot \min([\Delta x_i]^2 / [2N_{\text{dim}} D_i]) \quad (10)$$

where D is the diffusion coefficient of the processes included. At high resolutions or when D is large this limit may be prohibitive, and generally operator splitting methods combined with an implicit solver or super-time-stepping (Meyer et al. 2014) are required. While

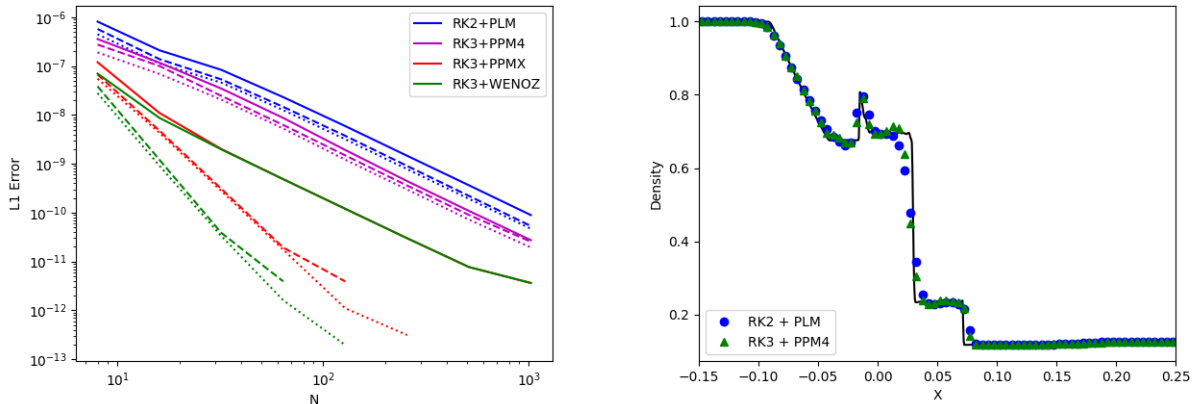


Figure 3. (Left) MHD linear wave convergence rates in 1D for fast (solid-line), slow (dashed-line), and Alfvén (dotted-line) waves for different methods. (Right) Density in the Brio-Wu shocktube test using 200 uniformly-spaced cells and different methods. The solid black line is a reference solution computed using 2000 cells and RK3+PPM4.

the generalized task list in `AthenaK` makes implementing these approaches straightforward, as of yet they have not been ported from `Athena++`.

To demonstrate the inclusion of diffusive terms in `AthenaK`, the right panel of Figure 5 shows the viscous diffusion of a Gaussian profile of the transverse component of velocity v_y in a 1D uniform grid at three different times, run on a single CPU core. The coefficient of viscosity $\nu = 1$, while the RMS width of the initial Gaussian $\sigma = 0.5$, giving a diffusion time of $\sigma^2/\nu = 0.25$. The analytic solution for this problem is also plotted as a solid line. The L_1 errors in the solution plotted in the left panel of the figure show convergence at second-order, as expected for the second-order finite differencing used to compute the viscous stress tensor Π . If higher-order integration methods are adopted, e.g. Felker & Stone (2018), then higher-order differencing of the diffusive fluxes must be used as well.

Figure 6 shows an MHD application with explicit viscosity and resistivity, namely the evolution of the magnetorotational instability (MRI) in 2D with no net vertical flux. With `AthenaK`, and using only 8 GPUs, it is possible to explore the dynamics at much higher resolutions, and therefore Reynolds numbers than previously possible. The calculation shown in Figure 6 using a resolution of 8192^2 and reaches a magnetic Reynolds number $Re_M = 10^6$, with a magnetic Prandtl number of 1. In idealized calculations of isolated current sheets it has been found that the magnetic reconnection rate becomes independent of Re_M when $Re_M \geq 10^5$ (Loureiro et al. 2012; Uzdensky et al. 2010), and reconnection enters the plasmoid-dominated regime. The zoom-in panel on the left of Figure 6 shows that after 10 orbits a large number of plasmoids have formed, although most of the current sheets in the flow are not associated with reconnection.

Currently this calculation is being repeated in full 3D at comparable resolutions and Reynolds numbers to investigate magnetic reconnection and turbulence driven by the MRI at high Re_M . Such calculations are only possible with codes that can exploit exascale resources.

3.4. Two-Fluid Magnetohydrodynamics

As discussed in §2, physics modules in `AthenaK` are included as independent objects in the `MeshBlockPack`, each with its own task list. This enables combining separate modules in the same calculation (for example multiple fluids, or a single fluid and the particle module described in §4). As a demonstration, we consider two-fluid MHD, in which both a hydrodynamic and an MHD module are included, with the momentum of the two fluids coupled through a collisional drag term

$$\mathbf{S} = \alpha \rho_i \rho_n (\mathbf{v}_i - \mathbf{v}_n) \quad (11)$$

where (ρ_i, \mathbf{v}_i) and (ρ_n, \mathbf{v}_n) are the mass density and velocity of the ions (MHD fluid) and neutrals (hydrodynamic fluid) respectively. This term is added to (subtracted from) the neutral (ion) momentum equations. Source terms to account for ionization and recombination, as well collisional drag heating, can also be included, however for simplicity we shall consider only non-reacting and isothermal fluids here.

Since the collisional drag term may become very large, the two-fluid equations of motion may be stiff, and the source term must be time-integrated implicitly. The system is therefore well suited for IMEX integrators, and in `AthenaK` we have implemented both second- and third-order IMEX integrators of Pareschi & Russo (2005), as well as the positivity preserving method described by Krapp et al. (2024). The left panel of Figure

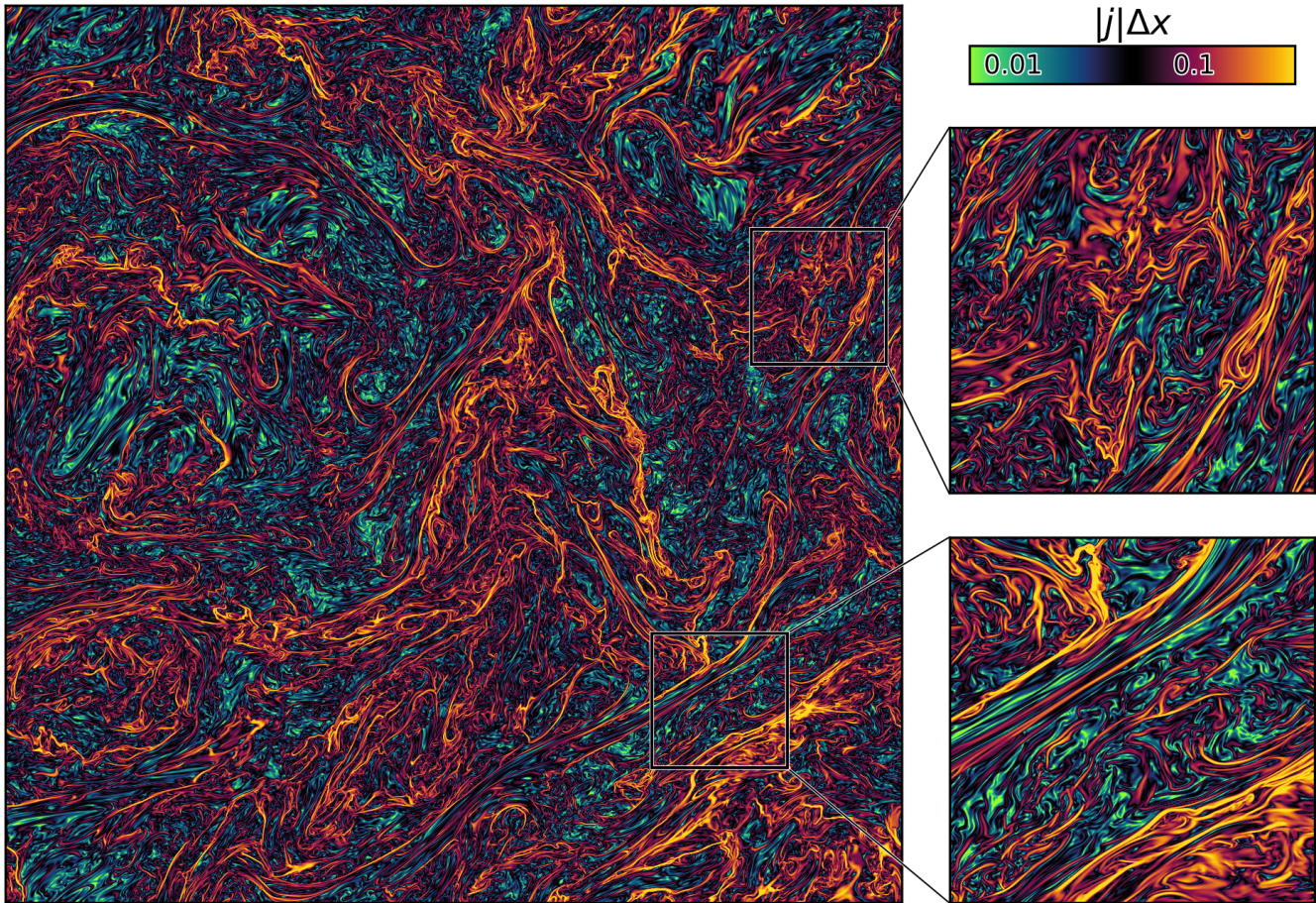


Figure 4. Magnitude of the current density in a 3D simulation of driven MHD turbulence at a resolution of 4096^3 . Insets show zoom-ins to selected regions.

7 shows a comparison of the second-order IMEX integrators using a 1D relaxation test. Two oppositely directed, equal density flows are initialized with $\rho_i = \rho_n = 1$ and $v_i = 1$ and $v_n = -1$, respectively. The initial plasma β is 1. The drag coefficient between ions and neutrals is set to $\alpha = 6 \times 10^3$. The two flows should rapidly come to equilibrium at rest. Data is output at every time step to follow this evolution. Note the IMEX2 integrator of Paeshi & Russo (2005) results in overshooting followed by damped oscillations toward the solution, whereas that of Krapp et al. (2024) smoothly converges to the correct result. Such overshoot can be very problematic when stiff source terms are added to the energy equation.

The right panel of Figure 7 shows the profile of the steady-state C-shock computed by Athena^K. The initial conditions are computed by solving the ODEs resulting from the assumption of time-independent equations of motion. This solution is mapped to a grid of 200 cells and then evolved with Athena^K for 10 flow times across the domain on a single CPU core. The

upstream initial conditions in the shock are $\rho_i = 10^{-3}$, $\rho_n = 1$, $v_i = v_n = 30$, with a transverse magnetic field $B_y/\sqrt{4\pi} = 10$, and collisional drag coefficient $\alpha = 1$. The upstream boundary conditions are held at these values, and the downstream boundary condition is out-flow. The isothermal sound speed $C = 1$ in both fluids, giving an upstream Mach number of 30, and Alfvén Mach number in the neutrals of 3. The characteristic width of the shock is the neutral-ion coupling length $V_{A,n}/(\alpha\rho_i) = 10^4$. The figure compares the final solution (points) with the initial conditions (solid line). The excellent correspondence between the two confirms the module correctly hold a steady C-shock profile.

Athena^K has already been used for new studies of isothermal two-fluid MHD turbulence in the ISM (Hu et al. 2024). Figure 8 shows typical results for the ionization fraction $f_i = \rho_i/(\rho_n + \rho_i)$ in a calculation using periodic boundary conditions, the IMEX3 time integration algorithm, and the PPM4 spatial reconstruction method. Initially, both the magnetic field and the ion and neutral density fields are uniform, with the mag-

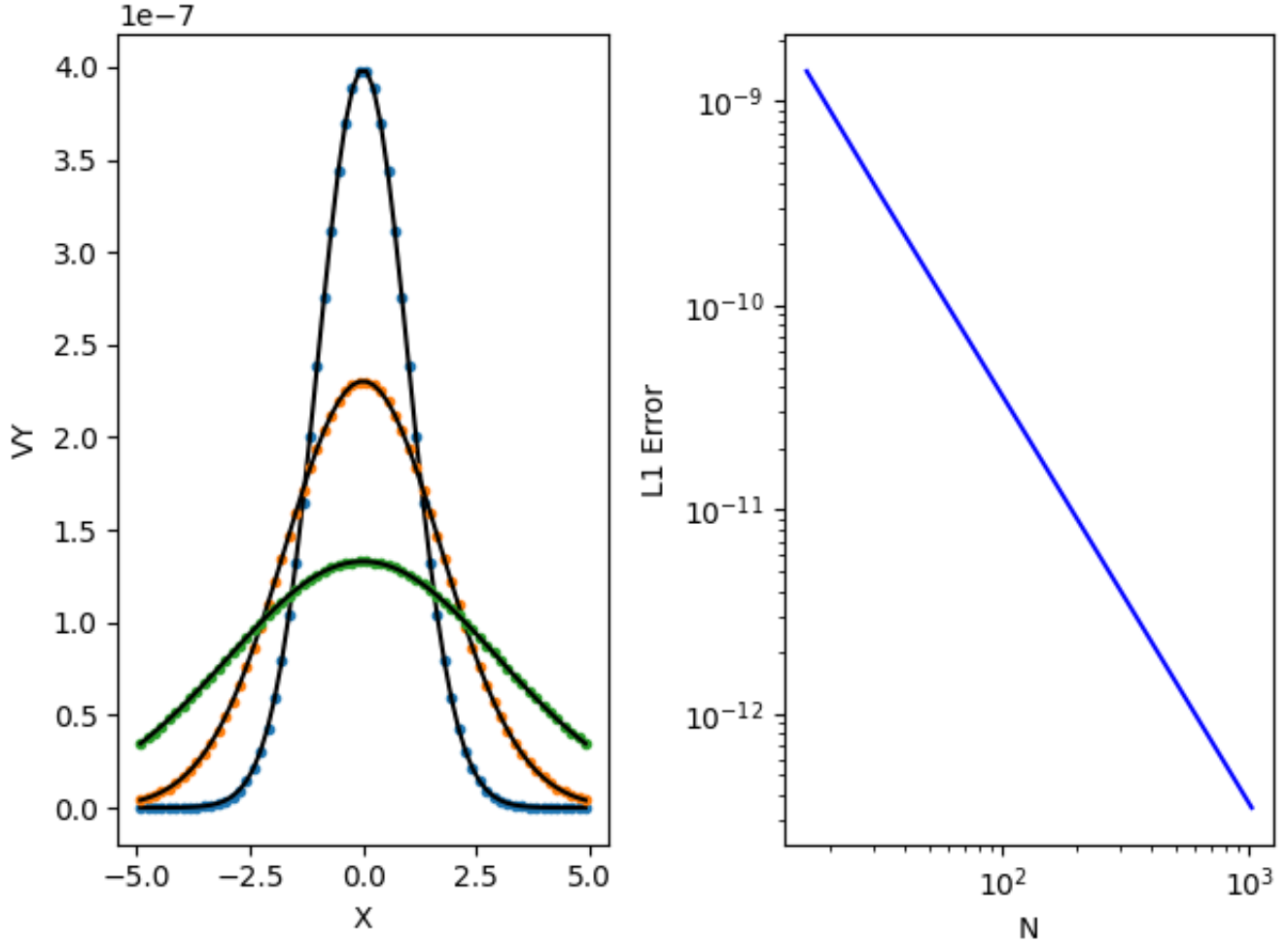


Figure 5. (Left) Viscous diffusion of a Gaussian profile of the transverse velocity v_y at times of 1, 2, and 4 using a 1D mesh of 64 cells. The analytic solution is given as a solid line. (Right) $\propto N^{-2}$ convergence of the L_1 error norm in this test.

netic field aligned along the z -axis. The initial ionization fraction is set to 0.1, and the drag coefficient between ions and neutrals is 10^6 . The simulation box is divided into 1200^3 uniform cells. Turbulence is driven solenoidally at wavenumbers $k = 1 - 2$ to achieve a Kolmogorov-like power spectrum. Snapshots were taken after the turbulence reached statistical saturation and the spectral slope was stable. The simulation ultimately achieves a sonic Mach number of $M_s \approx 10$ and an Alfvénic Mach number of $M_A \approx 1$. The image demonstrates that f_i can show complex fluctuations in two-fluid turbulence. An important result (Hu et al. 2024) is that the fluctuations in f_i can be of very large amplitude in some cases, although for the very strong coupling used in the calculation shown in Figure 8, the fluctuations are small.

3.5. Special relativistic hydrodynamics and MHD

In special relativistic MHD (SRMHD), assuming a unit system where $c = 1$, the conserved variables and their fluxes are

$$\mathbf{U} = \begin{bmatrix} D \\ \mathbf{M} \\ E - D \end{bmatrix}, \quad \mathbf{F} = \begin{bmatrix} D\mathbf{v} \\ \mathbf{S} \\ \mathbf{M} - D\mathbf{v} \end{bmatrix}, \quad (12)$$

where

$$D = \Gamma\rho, \quad (13)$$

$$E = \Gamma^2 w - \Gamma^2 (\mathbf{v} \cdot \mathbf{B})^2 - (p_g + p_m), \quad (14)$$

$$\mathbf{M} = (E + p_g + p_m)\mathbf{v} - (\mathbf{v} \cdot \mathbf{B})\mathbf{B}. \quad (15)$$

The stress tensor is

$$\begin{aligned} \mathbf{S} = & \Gamma^2 w \mathbf{v}\mathbf{v} - \frac{1}{\Gamma^2} \mathbf{B}\mathbf{B} - (\mathbf{v} \cdot \mathbf{B})(\mathbf{v}\mathbf{B} + \mathbf{B}\mathbf{v}) \\ & - \Gamma^2 (\mathbf{v} \cdot \mathbf{B})^2 \mathbf{v}\mathbf{v} + (p_g + p_m)\mathbf{I}, \end{aligned} \quad (16)$$

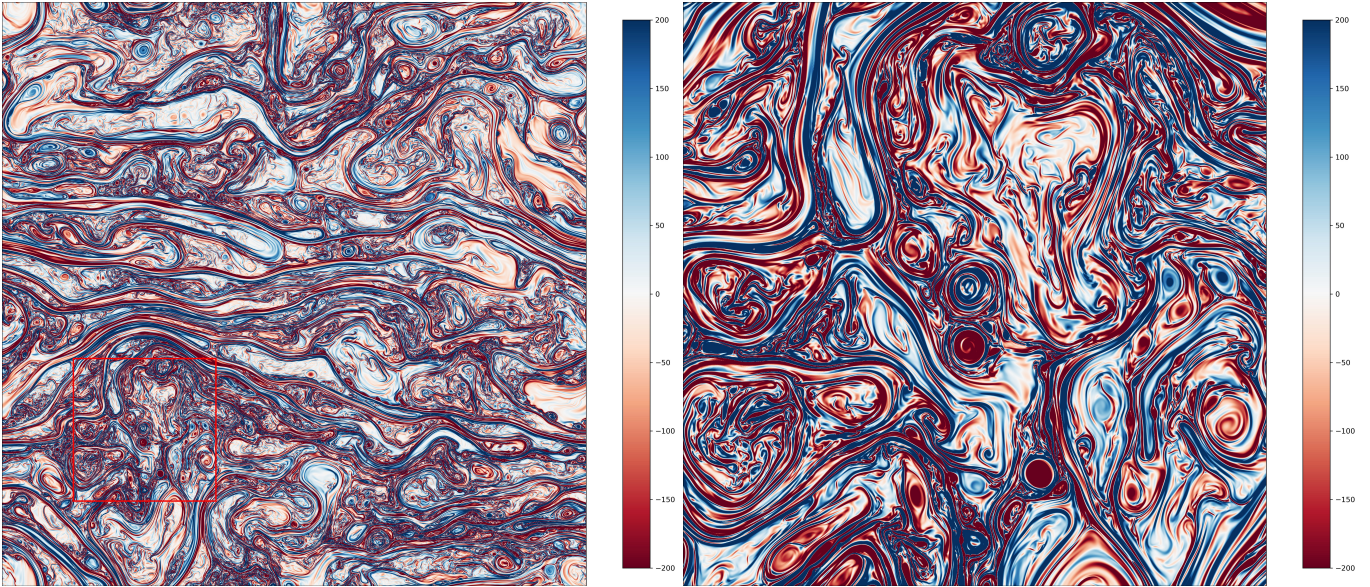


Figure 6. (Left) Out-of-plane component of the current density in a two-dimensional (axisymmetric) simulation of the MRI with no-net vertical flux, and with explicit resistivity and viscosity ($Re = Re_M = 10^6$) at extreme resolution. (Right) Zoom-in to the small region outlined in red in left image. Images are shown after evolving for 10 orbits.

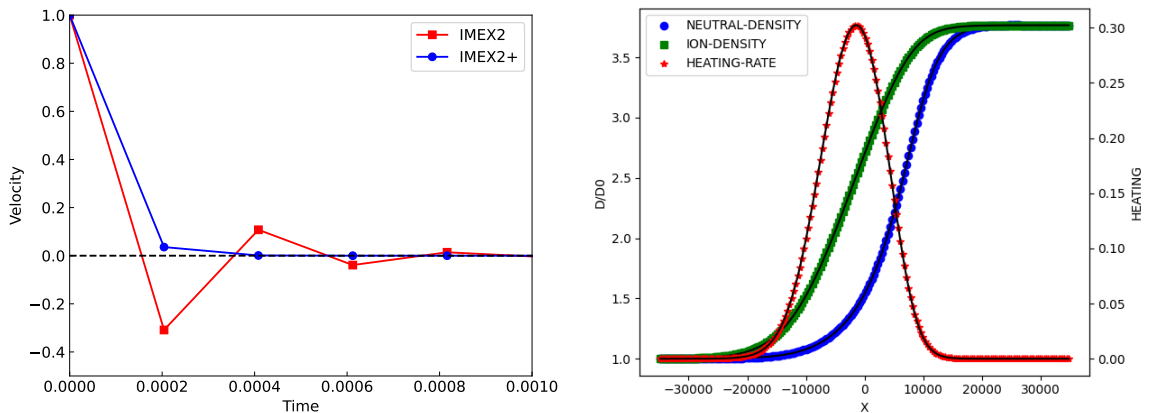


Figure 7. (Left) Decay of the ion velocity using second-order IMEX integrators when the drag source term is very stiff. (Right) Profiles of the ion and neutral densities, and per-volume heating rate in a C-type shock. Points are shown after 10 flow crossing times, while the solid lines are the initial conditions.

the total enthalpy is

$$w = \rho + \frac{\gamma}{\gamma - 1} p_g + 2p_m, \quad (17)$$

and Γ is the Lorentz factor (White et al. 2016; Stone et al. 2020). The gas pressure p_g is related to the gas internal energy u_g via a γ -law equation of state $p_g = (\gamma - 1)u_g$ and the magnetic pressure is

$$p_m = \frac{1}{2} \left(\frac{1}{\Gamma^2} \mathbf{B}^2 + (\mathbf{v} \cdot \mathbf{B})^2 \right). \quad (18)$$

We subtract the conserved density D from the total energy E in constructing our total energy conserved variable, in analogy to HARM's treatment of the total energy

equation (Gammie et al. 2003); this choice makes integrations more accurate in regimes where the magnetic and internal energy densities are much smaller than the rest mass density.

Special relativistic MHD in Athena^K invokes a primitive state vector $\mathbf{W} = [\rho, u^i, u_g]$, where u^i are the spatial components of the coordinate 4-velocity \mathbf{u} , related to the three velocity via $\mathbf{u} = \Gamma \mathbf{v}$. The conserved state vector \mathbf{U} can be analytically constructed from the primitive state vector \mathbf{W} , however, the inverse cannot. Here, in a departure from Athena++, we invoke the iterative conserved to primitive (C2P) solver of Kastaun et al. (2021).

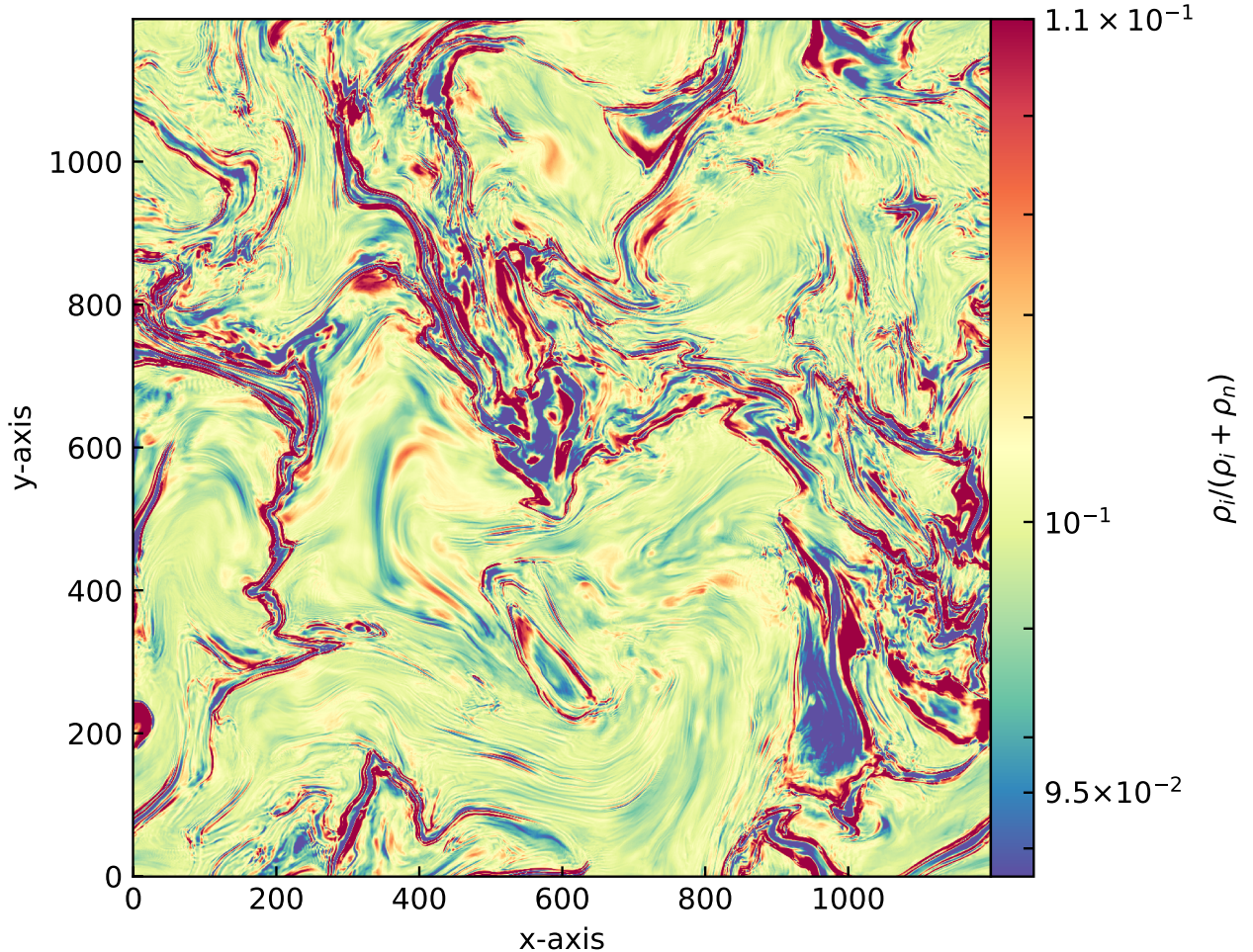


Figure 8. Slice of the ionization fraction in a 3D two-fluid simulation of compressible turbulence using a uniform grid of 1200^3 cells.

Figure 9 shows the results for a relativistic MHD blast wave test given in §4.3.1 of S20 as proposed by Mignone et al. (2012). The test uses AMR to capture the very thin shell formed by the relativistic dynamics. The initial conditions, grid, and AMR refinement criteria used in this test are identical to those described in S20, although here we use WENOZ reconstruction and the HLLC Riemann solver. The results are shown at a time $t = 0.4$ for direct comparison to Figure 37 in S08. Note that the shell is well resolved with AMR.

Komissarov (1999) devised a series of challenging SRMHD cylindrical blast wave test problems (invoking high $\sigma = 2p_m/\rho$ ambient backgrounds), where the relative “difficulty” of the problem is associated with the choice of initial (uniform) magnetic field strength B^x . Although mostly qualitative, the cylindrical explosion tests certainly challenge the robustness strategies of the SRMHD algorithm (including the C2P solver); many finite volume SRMHD codes require stringent

flooring, a modification to the background state (e.g., Leismann et al. 2005; Del Zanna et al. 2007; Beckwith & Stone 2011), and/or an artificial viscosity (e.g., Komissarov 1999) to evolve the problem. We find that first-order flux corrections (FOFC) enable us to integrate the problem robustly. Figure 10 shows AthenaK solutions for the cylindrical explosion tests, now supplemented with pressure-based AMR refinement. The blast is prescribed via an over-dense ($\rho = 10^{-2}$), over-pressurized ($p_g = 1.0$) region (within cylindrical radius $r \leq 1$), amidst an ambient background of gas density $\rho = 10^{-4}$ and pressure $p_g = 3 \times 10^{-5}$. An exponential ramp (see e.g., Mösta et al. 2014) is used to smoothly bridge the two regions. Figure 10 (left) and (right) correspond to initial field strengths of $B^x = 0.1$ and $B^x = 1$, respectively.

As an additional application for the SRMHD module, we study the formation of a strong shock inside a magnetar magnetosphere. It has recently been shown that

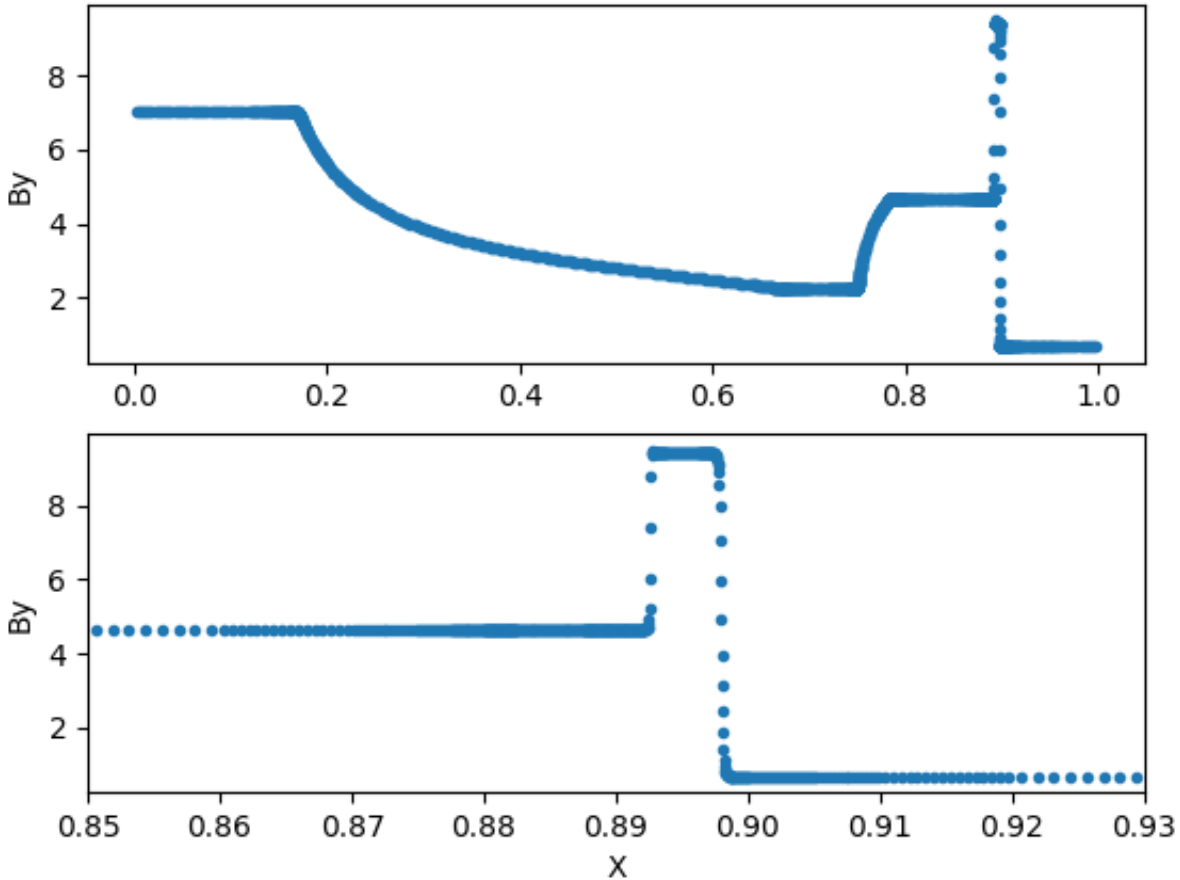


Figure 9. Transverse component of the magnetic field in the SRMHD shock tube test. Zoom-in shown in the bottom panel demonstrates how AMR can capture the very thin shell formed in this test.

magnetosonic fast waves inside MHD dipole magnetospheres can steepen into *monster shocks* (Beloborodov 2023). This can have implications for novel gamma-ray burst mechanisms from collapsing magnetars (Most et al. 2024), as well as for FRB mechanisms inside magnetar magnetospheres (Vanthieghem & Levinson 2024). Within the geometry of the dipole magnetosphere, this will happen when electric field toroidal component E_ϕ approaches the background magnetic field strength B . In a strongly magnetized magnetosphere with magnetization $\sigma = b^2/\rho \gg 1$ (where b is the magnetic field strength in the comoving frame), the limiting value of the magnetosonic speed c_s will be set by $c_s^2 \approx 1 - 1/\sigma$ (Beloborodov 2023). The fact that σ is finite is a requirement of the shock, as shock formation requires self-regulation of the shock by means of plasma heating. This makes simulations of monster shock formation extremely challenging, as it combines high Lorentz factors and magnetizations. We show the formation of a mon-

ster shock for an idealized two-dimensional scenario in Figure 11 using an 8192^2 mesh on a square domain with edges spanning $[-20, 20]$. For this simulation, we adopt a $\gamma = 4/3$ ideal fluid equation of state, setup a dipole magnetic field (as shown in Fig. 11), and initialize the temperature and density profiles by demanding that the magnetization parameters $\beta = 0.1$ and $\sigma = 40$ take uniform values.

In Figure 11, we show the early onset of shock formation. The shock forms when $E_\phi/B \rightarrow 1$. The shock resembles the simulation shown in Most et al. (2024). A full analysis of shock propagation, as well as on the dynamics of the shock will be provided in a separate study (Smith et al., *in prep*).

3.6. General relativistic hydrodynamics and MHD

Athena^K's general relativistic MHD (GRMHD) module evolves (assuming a unit system where $GM = c = 1$)

$$\partial_t \mathbf{U} + \partial_j \mathbf{F} = \mathbf{S}, \quad (19)$$

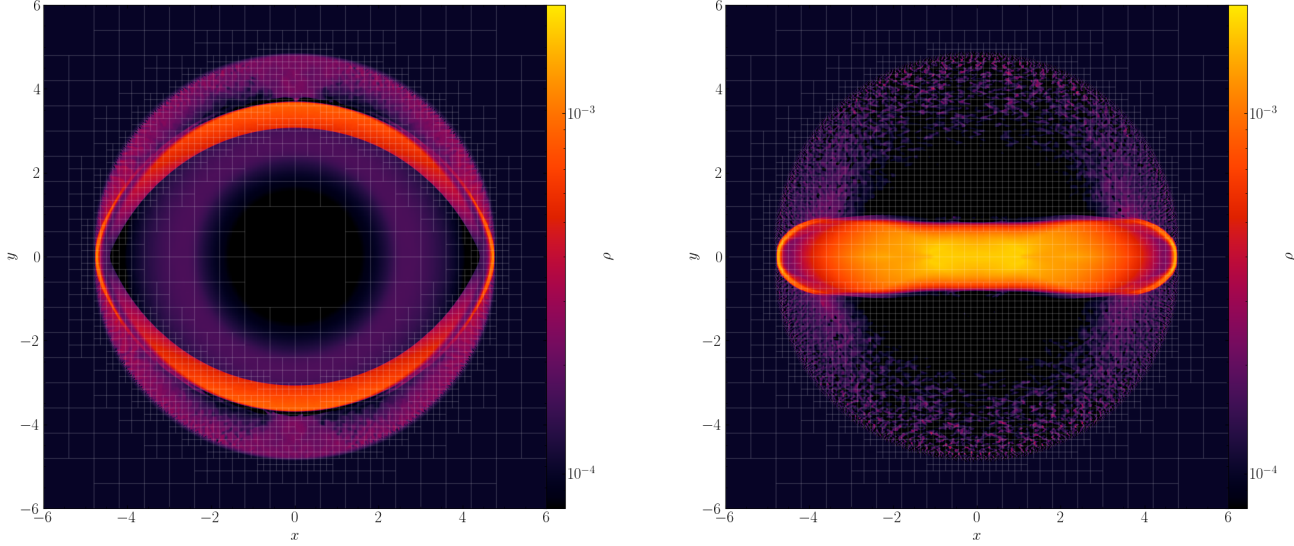


Figure 10. Logarithmic density ρ in the weak field ($B^x = 1/10$, left) and strong-field ($B^x = 1$, right) Komissarov (1999) cylindrical explosion tests, run on an AMR grid with pressure-based refinement. White lines denote 20×20 MeshBlock boundaries.

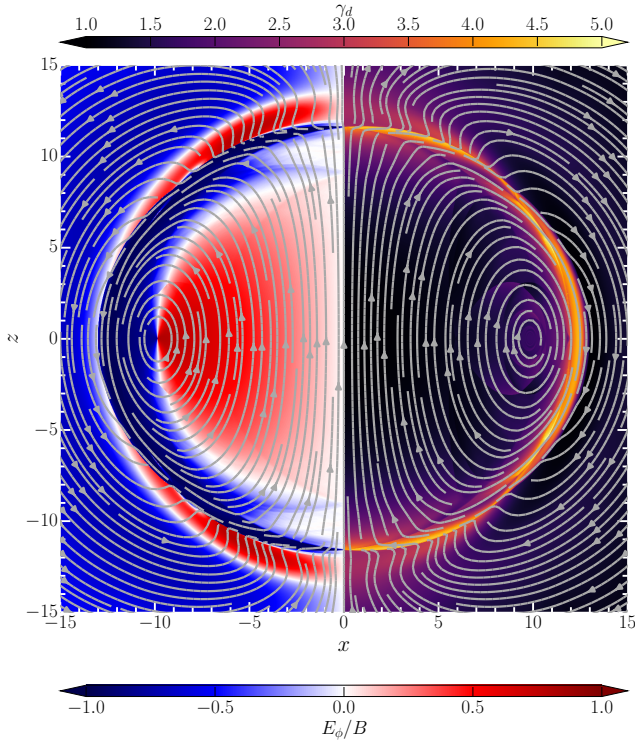


Figure 11. Formation of a monster shock inside a dipole magnetosphere (shown with grey lines). Shown are the drift Lorentz factor γ_d and the out-of-plane electric field component E_ϕ , normalized to the magnetic field B .

where the conserved variables, their fluxes, and source terms associated with the connection are

$$\mathbf{U} = \sqrt{-g} \begin{bmatrix} \rho u^t \\ T_i^t \\ T_t^t + \rho u^t \end{bmatrix}, \quad \mathbf{F} = \sqrt{-g} \begin{bmatrix} \rho u^j \\ T_i^j \\ T_t^j + \rho u^j \end{bmatrix},$$

$$\mathbf{S} = \sqrt{-g} \begin{bmatrix} 0 \\ \frac{1}{2} (\partial_i g_{\alpha\beta}) T^{\alpha\beta} \\ 0 \end{bmatrix}, \quad (20)$$

respectively, where $g = \det \mathbf{g}$ and \mathbf{g} is the metric, the rest-mass density is ρ , the coordinate frame 4-velocity is u^μ , the stress-energy tensor is

$$T_\nu^\mu = w u^\mu u_\nu - b^\mu b_\nu + (p_g + p_m) \delta_\nu^\mu, \quad (21)$$

the magnetic pressure is derived from the magnetic field b^μ via

$$p_m = \frac{1}{2} b_\mu b^\mu, \quad (22)$$

and w is the total enthalpy (Gammie et al. 2003; White et al. 2016; Stone et al. 2020). We again apply the HARM-“trick” (Gammie et al. 2003), wherein we eliminate contributions from the conserved density ρu^t from the evolved total energy conserved variable.

The GRMHD primitive state vector is $\mathbf{W} = [\rho, \tilde{u}^i, u_g]$, where \tilde{u}^i are normal frame, spatial velocity components, related to the coordinate frame velocity via $u^i = \tilde{u}^i - \beta^i \Gamma / \alpha$, where α , β^i , and Γ are the lapse, shift, and normal frame Lorentz factor, respectively. GRMHD

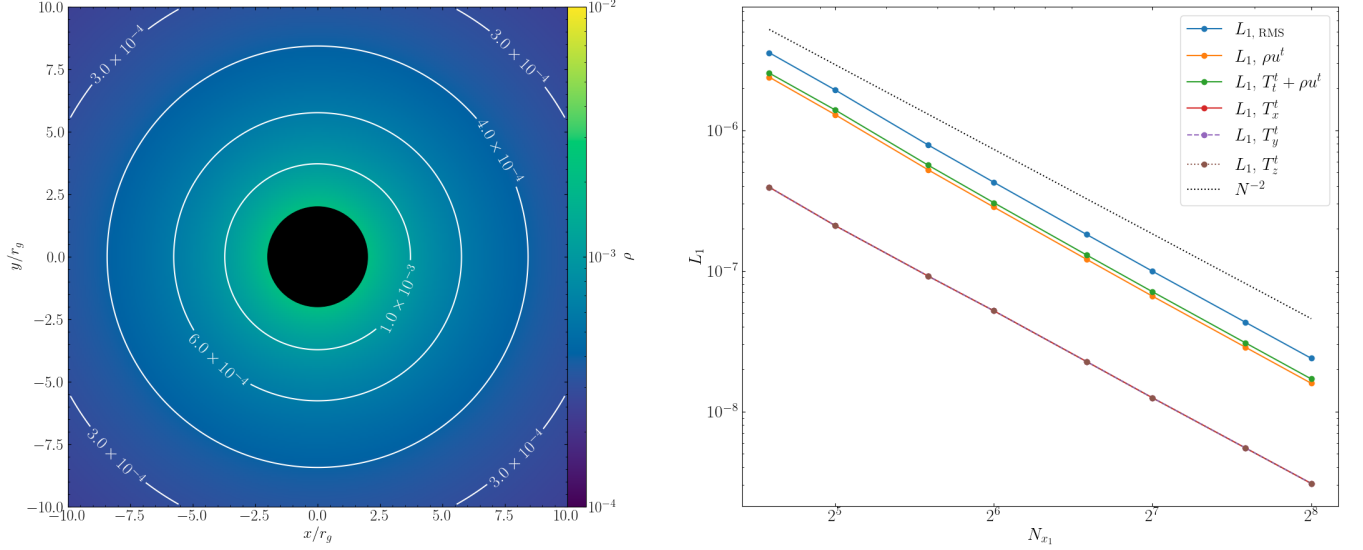


Figure 12. (Left): Logarithmic midplane density ρ (i.e., $z = 0$ slice) and contours from a spherically-symmetric Bondi accretion test problem; (Right): Convergence with numerical resolution for conserved variables $\rho u^t, T_\mu^t$; $\propto N^{-2}$ convergence is shown in dotted black.

shares the same [Kastaun et al. \(2021\)](#) C2P solver as SRMHD, supplemented only with the necessary frame transformations to cast the fluid state to the SR frame.

The GRMHD induction equation

$$\partial_t (\sqrt{-g} B^i) + \partial_j (\sqrt{-g} (b^i u^j - b^j u^i)) = 0 \quad (23)$$

evolves the magnetic field 3-vector components B^i subject to the no-monopole constraint

$$\partial_j (\sqrt{-g} B^j) = 0, \quad (24)$$

where B^i is related to the contravariant magnetic field b^μ via

$$b^t = u_i B^i, \quad (25)$$

$$b^i = \frac{1}{u^t} (B^i + b^t u^i). \quad (26)$$

Athena^K's GRMHD module is Cartesian only, invoking either the Cartesian Kerr-Schild (CKS; [Visser 2007](#)) or Minkowski metric, where both share $\sqrt{-g} = 1$. Following [Gammie et al. \(2003\)](#), Equations (19, 20) are presented in *free index down* form, hence giving rise to a conserved energy current. Because **Athena^K**'s GRMHD module operates in Cartesian only, our algorithm does not conserve angular momentum to machine precision as **HARM**.

When operating in CKS, an “excision” or “inner boundary” about the black hole is exercised (c.f., [Ressler et al. 2021](#); [Olivares et al. 2019](#)); **Athena^K** defaults to setting $\rho = \rho_{\text{excision}}$, $p_g = p_{g,\text{excision}}$, and $\tilde{u}^i = 0$ for $r \leq \frac{1}{2} (r_{h,\text{outer}} + r_{h,\text{inner}})$, where $r_{h,\text{outer}}$ and $r_{h,\text{inner}}$ are

the outer and inner horizon radii, respectively, evaluated in Kerr-Schild coordinates (hereafter, r, θ, ϕ).

Spherically-symmetric, Bondi accretion onto a Schwarzschild black hole is a common test problem for GR hydrodynamics codes; typically this test is performed in (spherical) Kerr-Schild coordinates (or modified variants thereof) *in 1D or 2D* (e.g., [Gammie et al. 2003](#); [White et al. 2016](#); [Porth et al. 2017](#); [Prather et al. 2021](#); [Chael 2024](#), to name a few). CKS coordinates require **Athena^K** to invoke a full 3D discretization for this problem. Our initial conditions (with black hole spin $a = 0$) are those prescribed by [Hawley et al. \(1984\)](#) and [White et al. \(2016\)](#), invoking a sonic point radius $r_c = 8M$, a polytropic index equal to the adiabatic index (i.e., isentropic) of $\gamma = 4/3$, and an adiabat $K = p_g/\rho^\gamma = 1$. Our simulation domain is cubic with edge lengths of $20M$. Outer boundary conditions are prescribed to the analytic solution. Our excision sets the primitive state vector to floors interior to the horizon ($r_h \leq 2M$), as previously detailed. For $r_h \leq r \leq 3M$, we reset the solution to analytic values after every integration stage — in this manner, noise introduced at the excision boundary does not enter our convergence analysis for all resolutions surveyed. Figure 12 (*left*) plots the rest mass density in an equatorial slice (i.e., $z = 0$) through the simulation domain after evolving the solution for $t = 100M$. We overplot contours to highlight **Athena^K**'s ability to preserve the spherically symmetric nature of the problem, despite operating in CKS coordinates. More quantitatively, Figure 12 (*right*) presents a convergence analysis demonstrating second order con-

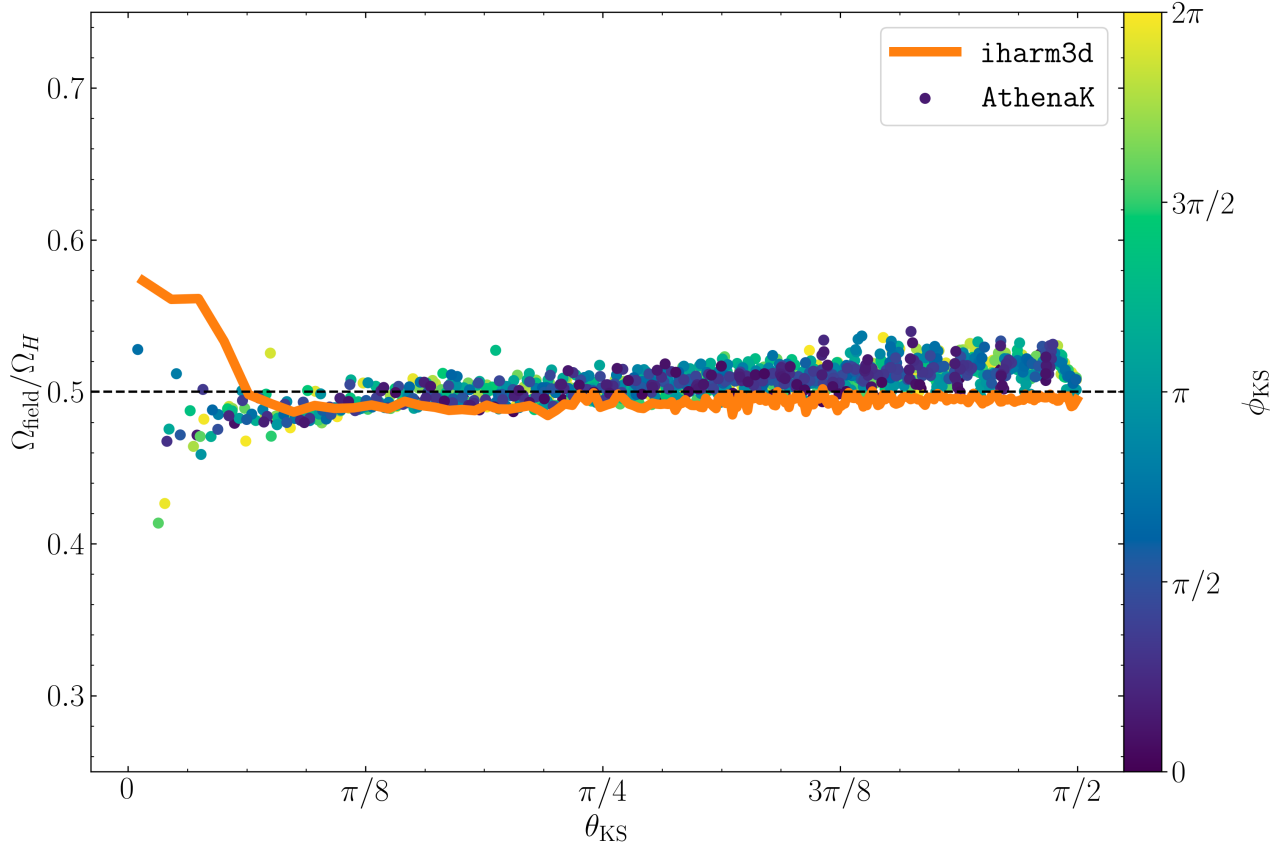


Figure 13. Field rotation rate Ω_{field} to horizon angular frequency Ω_H ratio measured at the horizon in a BZ monopole test problem (spin $a = 1/2$). Results from a 2D curvilinear `iharm3d` simulation are shown in orange. Results from a 3D CKS `AthenaK` simulation are shown at various θ, ϕ sample points. The expected solution $\Omega_{\text{field}}/\Omega_H \simeq 1/2$ is shown in dashed black.

vergence in L_1 errors of the conserved state vector when applying an RK2 temporal integrator, PLM reconstruction, and an HLLC Riemann solver.

Following [Chael \(2024\)](#), we next apply `AthenaK` to the so-called Blandford & Znajek (BZ; [Blandford & Znajek 1977](#)) monopole test problem. A monopole magnetic field $B^r \propto 1/r^2$ (initialized through a toroidal vector potential) threads a spherically symmetric medium prescribed via a density power-law

$$\rho(r) = \frac{(B^r)^2}{\sigma_c} \left(\frac{r}{r_c} \right)^{-n} \quad (27)$$

about a spin $a = 1/2$ black hole. We parameterize the gas pressure via $p = \rho T$ with $T = \gamma - 1$. We select $r_c = 10 r_{h,\text{outer}}$ and $n = -1$, which still corresponds to a density falloff with radius given the $\propto r^{-4}$ dependence on $(B^r)^2$. σ_c determines the ratio of the magnetic pressure to the gas density; we select $\sigma_c = 100$, which challenges `AthenaK`'s robustness strategies and primitive recovery scheme. At its heart, the BZ monopole problem tests our algorithm's ability to recover the expected

field rotation rate

$$\Omega_{\text{field}} = \frac{b^r u^\phi - b^\phi u^r}{b^r u^t - b^t u^r} \quad (28)$$

about the horizon, amidst a challenging fluid state subject to flooring, first order flux corrections, and/or C2P failure mitigation strategies. A $256 \times 256 \times 128$ grid resolves a domain with boundaries $x \in [-10M, 10M]$, $y \in [-10M, 10M]$, $z \in [0, 10M]$. Outflow boundary conditions are applied everywhere except the $z = 0$ plane, where we instead enforce reflecting boundary conditions. After evolving for $t = 10M$, we measure the field rotation rate Ω_{field} at the outer horizon by (1) interpolating the CKS primitive state vector to a surface $r = r_{h,\text{outer}}$, (2) converting to Kerr-Schild coordinates, then (3) evaluating Equation 28 at θ, ϕ sample points. In Figure 13, we plot $\Omega_{\text{field}}/\Omega_h$ where Ω_h is the rotation rate of the horizon. We overplot both the expected solution $\Omega_{\text{field}}/\Omega_h = 1/2$ and a solution generated with `iharm3D` ([Prather et al. 2021](#)).

Finally, we report `AthenaK` accretion rate histories for the SANE EHT code comparison run ([Porth et al. 2019](#)).

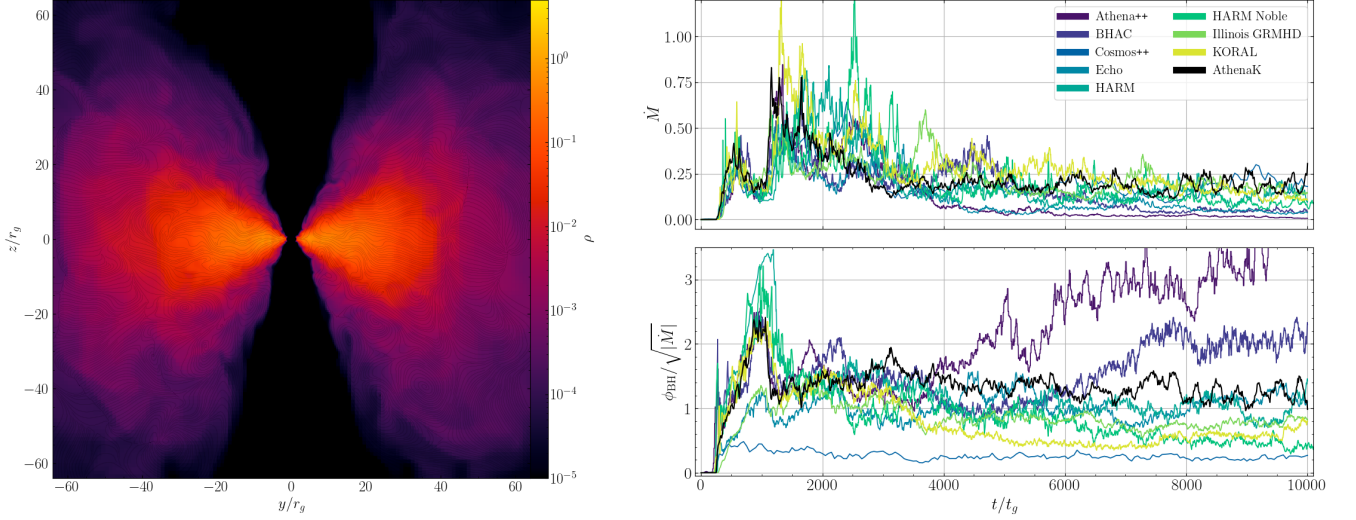


Figure 14. (Left): Snapshot of logarithmic density ρ in a poloidal slice through a SANE Fishbone-Moncrief torus about an $a = 15/16$ black hole evolved to $t \simeq 4000 t_g$; streamlines trace spatial components of the coordinate frame, contravariant 4-velocity (Right): Mass accretion rates \dot{M} and (normalized) magnetic flux $\phi_{\text{BH}}/\sqrt{|\dot{M}|}$ from the Porth et al. (2019), EHT SANE code comparison project are presented with **AthenaK** solutions overplotted in black.

A Fishbone-Moncrief (FM; Fishbone & Moncrief 1976) torus ($r_{\text{in}} = 6M$; $r_{\text{max}} = 12M$) is initialized about a spin $a = 15/16$ black hole. We match the code comparison project by (1) invoking a weak poloidal field loop initialized via a toroidal vector potential (with a strength parameterized by the global maxima of gas and magnetic pressures), (2) an adiabatic index $\gamma = 4/3$, (3) a 4% perturbation added to the gas pressure, and (4) evolving to $t = 10^4 M$. In Figure 14 (left), we plot a snapshot of the simulation at $t = 4000M$; the poloidal slice of the (logarithmic) gas density field is decorated with streamlines corresponding to spatial components of the coordinate velocity. Figure 14 (right) plots the **AthenaK** mass accretion rate \dot{M} and (normalized) magnetic flux at the horizon ϕ_{BH} alongside the 128³ datasets reported in Porth et al. (2019) for a suite of GRMHD codes. Many of the other codes surveyed in Figure 14 use logarithmic gridding to focus resolution near the horizon making a 1 : 1 comparison with our CKS grid less straightforward.

3.7. General relativistic radiation MHD

The *gray* (i.e., frequency integrated) photon transport equation in general relativity is

$$\begin{aligned} \partial_t [n^t n_t I] + \frac{1}{\sqrt{-g}} \partial_i [\sqrt{-g} n^i n_t I] \\ + \frac{1}{\sin \zeta} \partial_\zeta [\sin \zeta (n^\zeta n_t I)] \\ + \partial_\psi [n^\psi n_t I] = n_t (j - \alpha I), \end{aligned} \quad (29)$$

where I , j , and α are the frequency integrated specific intensity, emissivity, and absorptivity, respectively

(Davis & Gammie 2020; White et al. 2023). The (gray) specific intensity is defined in a *tetrad frame* and is a function of spacetime coordinates x^α and momentum space “angular” coordinates ζ (polar) and ψ (azimuthal). Components of \mathbf{n} help define directions in spacetime coordinates and momentum space, relating the tetrad frame and coordinate frame. **AthenaK** employs a *geodesic grid* (Randall et al. 2002; Wang & Lee 2011; Florinski et al. 2013; White et al. 2023; Daszuta & Cook 2024) to discretize solid angle Ω , tiling the unit sphere into hexagons and pentagons. The “level” of the geodesic grid determines the number of angles discretizing momentum space, $N_{\text{angles}} = 10N_{\text{level}}^2 + 2$.

The conserved variable for the transport equation is $\mathbf{U} = n^t n_t I$, with a corresponding flux \mathbf{F} having contributions from both a “spatial” operator (under ∂_i) and “angular” operators (under ∂_ζ and ∂_ψ). Fluxes are computed via simple upwinding. For the radiation source term $\mathbf{S} = n_t (j - \alpha I)$, **AthenaK** decomposes the frequency integrated emissivity and absorptivity into absorption and scattering components, where the former assumes the gray form of Kirchoff’s law (hence assuming LTE) and the latter assumes *fluid frame* isotropic, elastic scattering. Only *constant* or *power-law* (i.e., Kramers-like) specific absorption opacities κ_a and/or *constant* specific scattering opacities κ_s are currently supported. In an operator split update, a locally-implicit, backward Euler discretization advances the fluid frame specific intensity due to absorption and/or scattering. Radiation talks to the fluid sector through

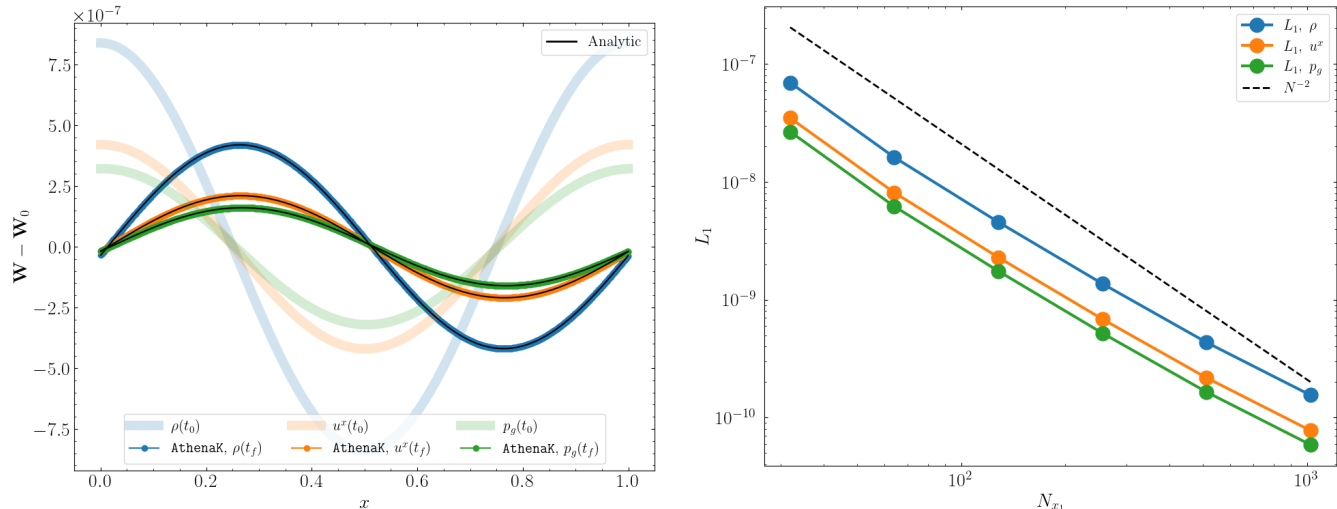


Figure 15. (Left): **AthenaK** primitive solutions \mathbf{W} for a radiation-modified linear wave test problem at initial time t_0 and final time t_f ; fluid frame density ρ , coordinate frame 4-velocity spatial component u^x , and fluid frame gas pressure p_g are shown in blue, orange, and green respectively; analytic solutions are presented in black. (Right) Convergence with numerical resolution for primitives \mathbf{W} ; $\propto N^{-2}$ convergence is shown in black.

its moments

$$\partial_t T_\mu^t = -\partial_t R_\mu^t, \quad (30)$$

where $R_\mu^t = \int n^t n_\mu I d\Omega$ are the coordinate frame radiation moments. Following the operator split update for the radiation source term, we conservatively update the fluid four-momentum via changes in R_μ^t .

Figure 15 shows **AthenaK** numerical solutions (*left*) and a convergence analysis (*right*) for a gas-dominated, radiation-modified linear wave test in Minkowski space, as described in [White et al. \(2023\)](#). We must invoke a single-angle-per-octant angular grid for this test problem so that $R^{\mu\nu} \propto \text{diag}[1, 1/3, 1/3, 1/3]$ (i.e., Eddington) is exactly recovered (as assumed by the analytics). Figure 15 (*left*) shows the primitive state vector \mathbf{W} for (1) the initial condition (*translucent*) and at (2) a final time (*opaque*), characterized as the time when the seeded linear perturbation decays by a factor of 2. Analytic solutions are overplotted in black. Figure 15 (*right*) shows the corresponding convergence analysis, decomposing the L_1 errors into contributions from the mass density ρ , coordinate frame 4-velocity spatial component u^x , and gas pressure p_g . $\propto N^{-2}$ convergence is overplotted in dashed black, but we remark that the expected convergence rate for this problem is non-trivial. We apply the RK2 temporal integrator with PLM reconstruction for both the hydrodynamics and radiation sector, corresponding to an overall 2nd order error associated with advection (we note that radiation “angular” fluxes are zero for this problem); however, **AthenaK**’s backward Euler, operator split discretization for the radiation source term limits our algorithm to be only first

order accurate in time. The better-than-first-order convergence in Figure 15 (*right*) is a testament to the dominance of advection errors for this gas-dominated linear wave. We refer readers to [White et al. \(2023\)](#) to see the convergence behavior associated with radiation-modified linear waves in different regimes. Albeit we here only present solutions in 1D, we have confirmed that **AthenaK** can recover analytics in 3D when inclining the wavevector to the grid (akin to [Gardiner & Stone 2008](#)), as long as the angular grid is equally rotated to enforce Eddington.

Figure 16 shows **AthenaK** solutions for vacuum transport in the Schwarzschild metric (c.f., [Sądowski et al. 2013](#); [Anninos & Fragile 2020](#); [Asahina et al. 2020](#); [White et al. 2023](#)). Radiation is injected along the photon orbit ($r = 3M$) around a non-spinning black hole, with a beam opening width of $0.7M$ (proper distance) about the injection point and a (half-)opening angle of 10° . The angular resolution for this problem is defined in terms of the mean number of angles resolving the solid angle of the beam for illuminated cells, $N_{\text{avg}} = 144$. The spatial resolution is $\Delta x = \Delta y = (1/32)M$. Lime green lines depict the beam injection area and analytic geodesics for the beam inner and outer boundaries. Numerical diffusion of the beam outside the analytic boundaries are associated with truncation error in the spatial and “angular” transport operators. The error is likely dominated by our “angular” fluxes, which invoke donor cell reconstruction; spatial fluxes invoke PLM.

Finally, Figure 17 highlights a sample production calculation run on OLCF’s Frontier using **AthenaK**’s

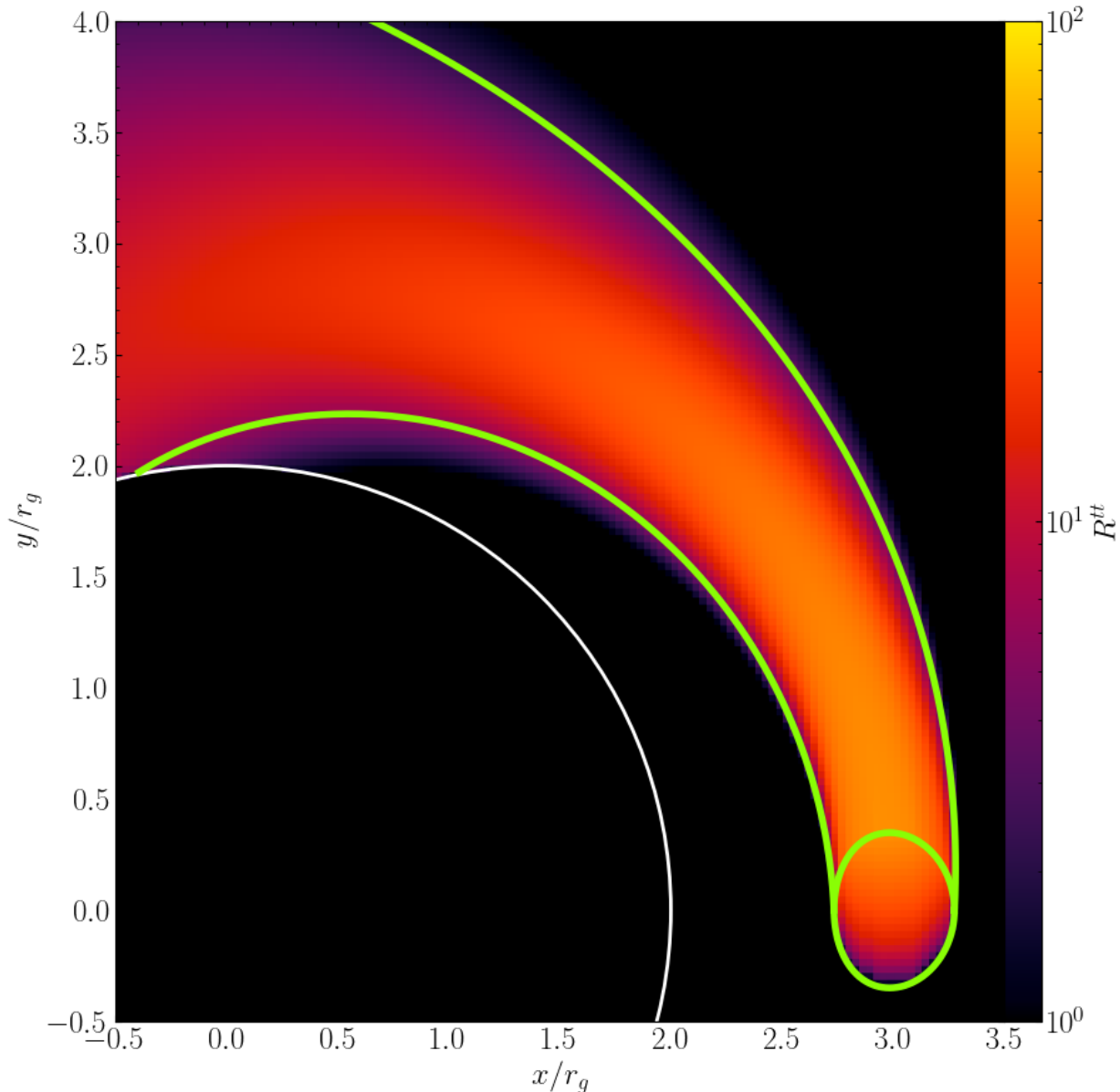


Figure 16. Beam propagation in the Schwarzschild metric. Color shows logarithmic, coordinate frame radiation energy density R^{tt} for an equatorial beam injected along the photon orbit. Lime green tracks geodesics along beam boundaries; white traces the event horizon.

diation GRMHD module. A tilted (45°) Chakrabarti torus (Chakrabarti 1985) is initialized in \sim hydrostatic and thermal equilibrium about an $a = 15/16$ black hole. A weak poloidal loop threads the torus. An $N_{\text{level}} = 2$ geodesic grid (42 angles) discretizes momentum space. A nested SMR grid is used to focus resolution about the horizon. A density unit is selected such that the absorption and scattering opacities lend the system to a sub-Eddington accretion rate. At $t \simeq 6500M$, the MRI is well-developed in the tilted accretion disk, and a thin, overdense midplane forms due to strong radiative cool-

ing. MRI- and radiation-mediated angular momentum transport drive mass accretion in the system; GR effects produce a black-hole-spin-aligned, inner accretion disk, while the outer disk remains misaligned (Bardeen & Petterson 1975; Papaloizou & Pringle 1983).

4. PARTICLE MODULE

In addition to the fluid solvers described above, a module for integrating the motion of particles in various regimes has been implemented in Athena^K. This module is similar to the particle module implemented in

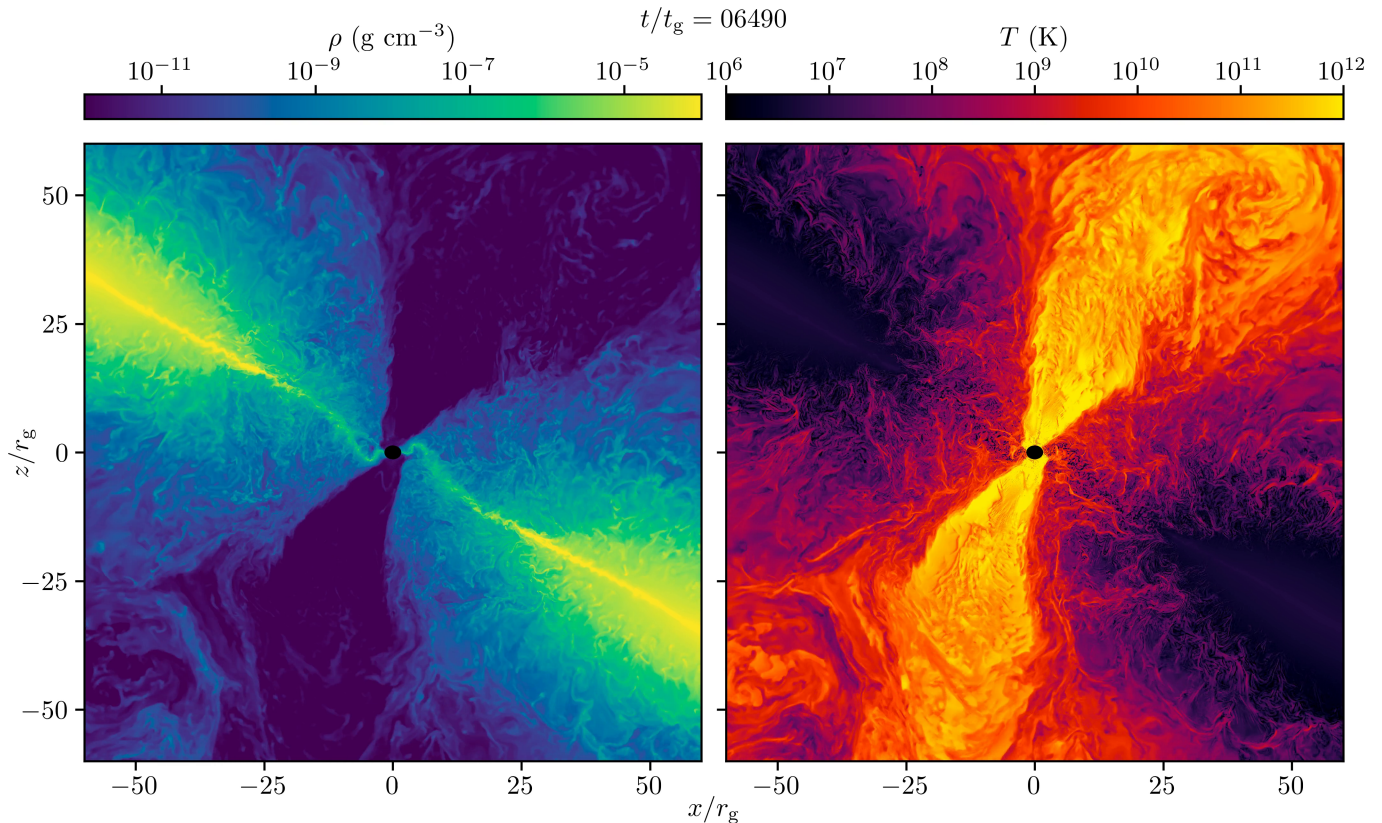


Figure 17. Logarithmic fluid frame mass density ρ (left) and gas temperature T (right) in a poloidal slice through a tilted (45°), sub-Eddington accretion disk about an $a = 15/16$ black hole.

Athena++ for evolving dust particles (Bai & Stone 2010) and cosmic rays (Bai et al. 2015), which was used as the basis for the *Pegasus* hybrid-PIC code (Kunz et al. 2014). However, there are some important differences.

In *AthenaK* an arbitrary number of `double` and `int` data for each particle can be stored in `2D Views`. Each rank stores the data for all particles located within the `MeshBlocks` in its `MeshBlockPack`. Given the `MeshBlock` ID and coordinates of a particle, it is very easy to calculate the integer indices of the cell containing that particle on the regular Cartesian mesh. This makes interpolating cell data to the particle positions straightforward.

Communication of particle data between MPI ranks proceeds as follows. At each time step, a list of all particles that will move beyond the boundaries of the `MeshBlocks` stored on the rank is created, and using the AMR binary tree, the ID of the new `MeshBlock` the particle will enter is found. This information is then shared amongst all ranks using a gather-scatter operation. Once all ranks have the list of all particles that need to be communicated and their destination, it is simple to calculate how many particles must be sent to or received from each rank, and to post non-blocking MPI sends and receives for the particle data. Particle

data is added and removed from the `2D Views`, which are resized as necessary. The use of gather-scatter operations is a significant design difference from the manner in which particles are communicated in *Athena++*, and helps to reduce the total number of messages communicated.

Particle data can be output in a variety of formats, including the VTK single-point type which can be read by many standard visualization tools. In addition, selected particles can be labelled as tracers, with the mesh data at the location of the particle output to a custom file format at a user-defined interval. This is very useful for tracing the time-history of the flow sampled by particles.

Other than the data, communication, and I/O infrastructure, the only other ingredients to the particle module are a pusher to integrate the motion of the particles, and a method to interpolate/deposit grid data to particles/cells. These depend on the types of particles used, and are described in the subsections below.

4.1. Lagrangian tracer particles

Rather than updating particle positions by interpolating the fluid velocity to the location of the particle, Genel et al. (2013) describes an alternative method to probabilistically move particles according to mass fluxes

computed during the fluid evolution step. In this ‘‘Lagrangian Monte Carlo’’ approach, particles are localized only to an individual zone rather than to a precise position within the domain and are probabilistically moved between zones according to the finite-volume conserved mass fluxes through faces between neighboring zones. This method forces the particles to follow the fluid flow (up to statistical noise and diffusion), which lies in contrast to velocity update methods, which have been shown to yield to misrepresentative mass distributions and measures of the fluid power spectrum (Genel et al. 2013).

Particle positions are updated at each time step. In each cell, the outgoing mass fluxes through cell faces are taken from the fluid calculation and normalized by the conserved mass in the source cell. A random number is then generated for each particle within the cell and used to select whether the particle should remain in the cell or be moved to one of the neighbors according to the normalized outgoing fluxes. Particles are moved between `MeshBlocks` as described above; however, an extra post-transfer step is required when a particle moves into a `MeshBlock` at a different refinement level. If the refinement level of the new `MeshBlock` is less than the original refinement level, the particle is simply moved into the center of the corresponding cell. When the new `MeshBlock` refinement level is greater than the original refinement level, a random number is generated and used to select which of the four refined cells the particles should be moved into according to the relative ratio of (corrected) mass fluxes into each of the refined cells.

Figure 18 compares the distribution of a passive contaminant advected with the fluid flow to a set of 10^7 Lagrangian Monte Carlo tracer particles during the development of the Kelvin-Helmholtz instability (KHI) in 2D. The initial condition for this test problem is from Lecoanet et al. (2016) and uses $P_0 = 10$, shear velocity of 1, width of shear profile $\sigma = 0.2$, $a = 0.01$. The fluid solution is computed using the LLF Riemann solver with PLM spatial reconstruction and the RK2 temporal integrator within a 2D domain with resolution 512×1024 for $-0.5 < x < 0.5$ and $-1 < z < 1$. The passive contaminant is initialized according to (8e) of Genel et al. (2013); and its state is shown at times $t = 2$ and $t = 3$ as computed by the fluid equations (top row) and as recovered from the Lagrangian tracer particles (bottom row).

While the Lagrangian Monte Carlo method more accurately follows the mass flow and better recovers the statistical properties of the underlying fluid, it is more diffusive than the fluid evolution itself. The extra diffusivity is a fundamental consequence of the probabilistic

update algorithm, results in an effective random walk with respect to the true history of the particles, and cannot be mitigated by increasing the number of particles. In practice, this means that the tracer particle histories may be interpreted as being noisy (see Genel et al. 2013).

4.2. Test particles

For many problems it is of great interest to follow the motion of charged test particles in the magnetic field produced by an MHD flow, for example to understand cosmic ray scattering by turbulence in the ISM, or the acceleration of particles in accretion disk turbulence. In Athena_K such motion can be computed either from static snapshots of the flow in a post-processing mode, or dynamically by evolving both the MHD and particle motion simultaneously to capture the effect of intermittent structures. The former is well motivated in the study of cosmic ray scattering by inter-stellar turbulence, as typical inter-stellar gas velocities are several orders of magnitude smaller than the speed of light. In the latter case the ratio of the velocity of the particles compared to the fluid must be limited.

To integrate the motion of the particles, various pusher functions have been implemented in Athena_K, including a method based on the Boris algorithm to conserve the magnetic moment of particles (Boris 1970), and a method for orbital integration in general relativistic curved spacetimes (Bacchini et al. 2019). The MHD fields are evaluated at the particle positions from the grid using either a linear interpolation method or the Triangular Shaped Cloud interpolation method (Birdsall & Langdon 1991).

As an example, Figure 19 shows the motion of select particles in isothermal, driven MHD turbulence on a 1280^3 grid with a Reynolds number of 5×10^4 and a magnetic Prandtl number of 1. The turbulence simulation uses an HLLD Riemann solver and the same driving and spatial reconstruction as the 4096^3 turbulence simulation described in §3.2 and Figure 4. After ≈ 7 outer-scale eddy turnover times with steady-state $\delta B/\bar{B} \approx 3$, the turbulent field was restarted in static post-processing mode and $\approx 3.6 \times 10^7$ charged-particle trajectories were integrated for over 6 additional box-crossing times. The white and cyan lines in Figure 19 show example particle trajectories for two different charge-to-mass ratios (white lines corresponding to twice the charge-to-mass ratio of the cyan lines). The background shows the magnitude of the current density normalized by the grid spacing in three 2D slices through the 3D domain, highlighting the intermittency of the fields through which the particles propagate.

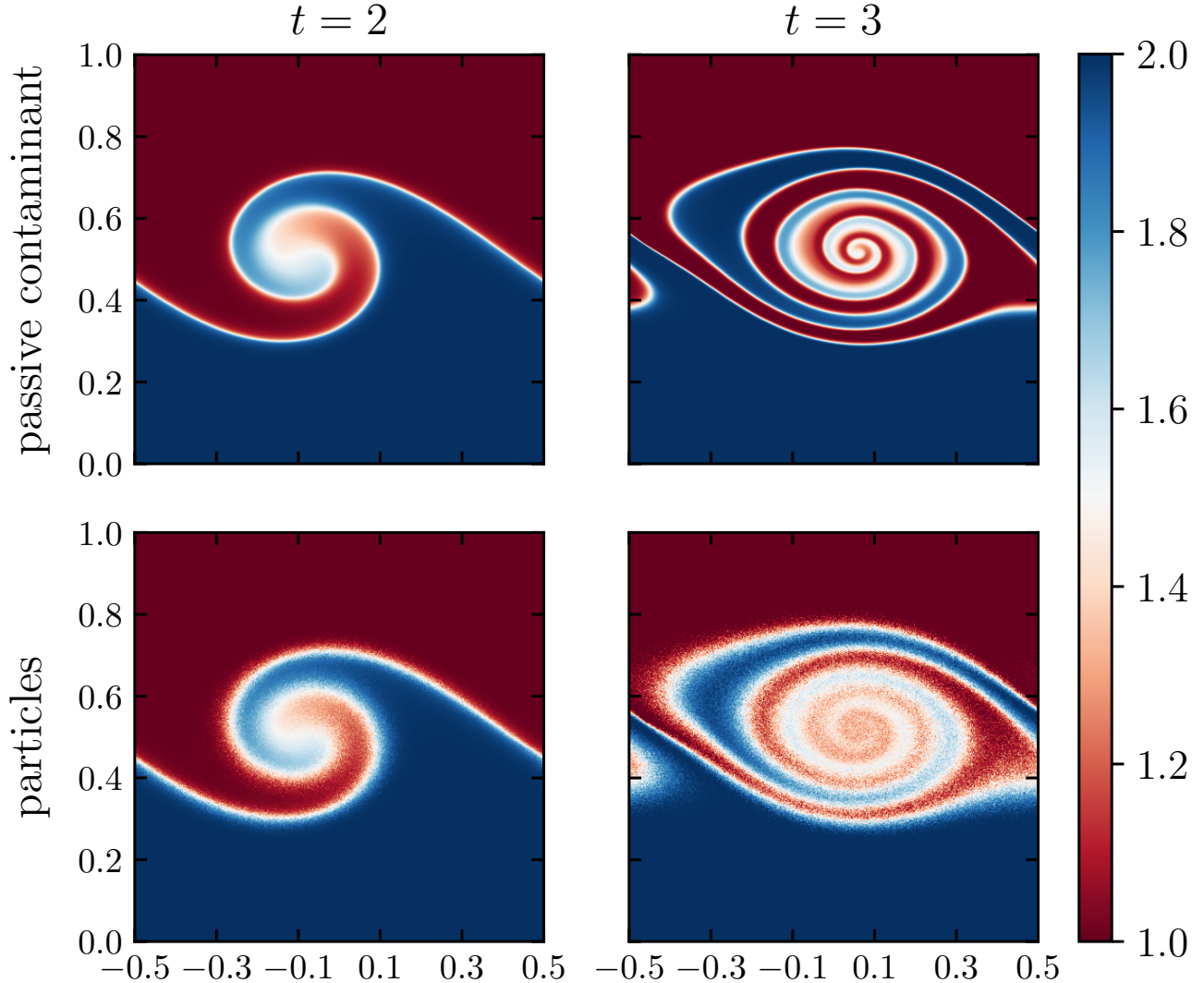


Figure 18. Passive contaminant (top row) and Lagrangian tracer particles (bottom row) in the [Lecoanet et al. \(2016\)](#) KHI test.

5. PERFORMANCE AND SCALING

A primary motivation for developing **AthenaK** has been to use **Kokkos** to enable performance portability, and it is important to test if this goal has been achieved. In this section we present the results of performance and weak scaling tests on various architectures.

5.1. Single-Device Performance

Table 1 shows the performance on a variety of devices (measured in cell-updates-per-device-second) of the Newtonian hydrodynamics and MHD solvers running a linear wave convergence test on a uniform mesh. On CPUs, the mesh consists of a single 128^3 **MeshBlock**, and the test is performed using all cores available on a given CPU. Since the performance of **AthenaK** on CPUs

is typically memory bandwidth limited, this represents a more realistic measurement appropriate to actual applications. On GPUs, we use a $512 \times 256 \times 256$ grid tiled with 128^3 **MeshBlocks**. The table demonstrates **AthenaK** is achieving excellent performance across the full range of devices tested. On CPUs, the performance is comparable to that reported for **Athena++** (S20). The latter included aggressive vectorization of loops using compiler directives, while in **AthenaK** we rely on **Kokkos** **cmake** options to enable these options. It is likely that further optimizations of **AthenaK** targeting CPUs is possible. On GPUs, the performance shown in Table 1 is comparable to, or better than, other GPU hydrodynamic and MHD codes reported in the literature, for example **ChollaMHD** ([Caddy & Schneider 2024](#))

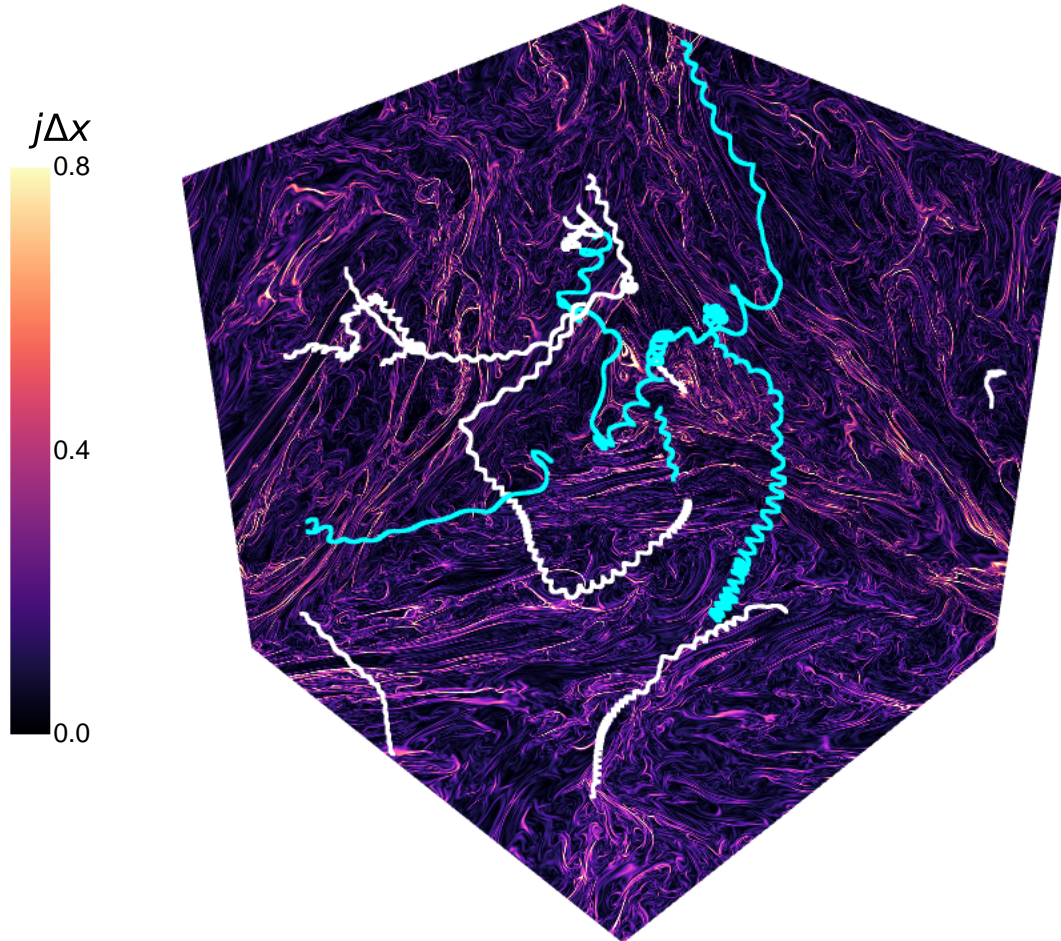


Figure 19. Current density (background colors) and charged particle trajectories for two different charge-to-mass ratios (cyan and white lines) in a 3D simulation of driven MHD turbulence at a resolution of 1280^3 .

Table 1. Performance of Athena κ on various devices

	Apple M1 pro (8 cores)	Intel Xeon Gold 6326 (32 cores)	NVIDIA V100	NVIDIA A100	AMD MI250	NVIDIA H100	NVIDIA Grace Hopper
hydro	34	63	298	614	405	677	1077
MHD	11	33	158	298	190	290	565

or AthenaPK (Holmen et al. 2024). On the latest generation of devices, the NVIDIA Grace Hopper processor, Athena κ achieves more than 10^9 cell updates per second per device for 3D hydrodynamics.

As discussed in S20, we find the size of the MeshBlocks has a significant effect on the measured performance. For example, on an NVIDIA A100, reducing the MeshBlock size to 64^3 , 32^3 or 16^3 while keeping the overall grid the same reduces performance from 614 Mzc/s

to 413, 242 and 126 Mzc/s respectively. Precisely the same behavior was observed on CPUs using Athena++, albeit for smaller MeshBlock sizes. It is clear that for best performance it is important to tune the size of the problem to the capability of the target device. Running small problems on GPUs is not an effective use of resources.

To investigate the relative performance of the different physics solvers, Table 2 shows the performance of each

Table 2. Performance of various solvers in **AthenaK** on selected devices

	Hydro	MHD	SR-hydro	SR-MHD	GR-hydro	GR-MHD	rad-GR-hydro
Intel Xeon Gold 6326	63	33	16	20	13	12	6.2
NVIDIA A100	614	298	378	178	281	120	109
NVIDIA GH	1077	565	653	297	445	227	211

on selected devices. For non-relativistic problems the performance is measured using the same linear wave convergence test as used for Table 1, while for SR and GR a 3D shocktube problem is used. For non-relativistic, SR, and GR fluids the MHD solver runs roughly $2\times$ slower than the equivalent hydrodynamic solver on most devices, due to the extra complexity of the Riemann solvers and the cost of integrating the induction equation with CT. The exception is for SR hydrodynamics on CPUs, which runs slower than SRMHD. In SR and GR, the nonlinear root finding algorithm required to compute the primitive variables can add significant cost. Likely this algorithm requires further tuning on CPUs. Again, **AthenaK** shows performance similar to other codes published in the literature, for example reaching 120 Mzcps for GRMHD on an NVIDIA A100, which is comparable to the performance reported for the highly optimized H-AMR code (Liska et al. 2022).

An important capability of **AthenaK** is the AMR framework, and to demonstrate that the block-based AMR strategy adopted in the code can be run effectively on heterogeneous systems such as GPUs, we have run a 2D MHD blast wave test on a single NVIDIA A100 GPU. The initial conditions consist of a uniform background with constant density and pressure to which a circular region with pressure $100\times$ the background is added. The test is run with both a uniform 4096^2 grid with 64^2 **MeshBlocks**, as well as with AMR on a 1024^2 root mesh with 64^2 **MeshBlocks** and a maximum of two levels of refinement (so as to achieve the same resolution as the uniform mesh). Refinement occurs wherever the density exceeds the background by a factor of 1.1. Figure 20 shows that the resulting density profiles are essentially identical, confirming the fidelity of the AMR algorithm. Most importantly, using block-based AMR on GPUs only incurs a roughly 20% overhead: the uniform mesh calculation runs at 181 Mzcps, while the AMR calculation runs at 141 Mzcps. In fact this overhead is likely amplified by the use of a 2D mesh, which significantly reduces the work associated with each **MeshBlock** (a 3D version of this test is too large to fit on a single device). Nevertheless, the AMR calculation is significantly more efficient than using a uniform mesh, requiring only 18% of the wall clock time. This reduction results both

because of the smaller number of **MeshBlocks** needed with AMR and a larger timestep due to the coarser grid where the wavespeeds are maximal.

Overall, we find the AMR framework implemented in **AthenaK** using **Kokkos** achieves comparable performance to similar algorithms implemented in vendor specific programming models. We conclude **Kokkos** has indeed enabled performance portability.

5.2. Weak Scaling

To test the parallel scaling of **AthenaK** on modern exascale HPC systems, we have performed weak scaling tests on both Perlmutter at NERSC (composed of NVIDIA A100s) and Frontier at OLCF (composed of AMD MI250X). Figure 21 shows the total performance (in Mzcps) and parallel efficiency (defined as performance per device compared to the performance on a single device) for both hydrodynamic and MHD linear wave convergence tests run on both machines. On Perlmutter there is a significant drop in performance when using a small number of nodes, however for larger jobs the parallel efficiency recovers to roughly 70% on 4096 GPUs. We note that both machines are in production mode with a heavy workload, and this likely affects the way that small jobs are distributed on the network. On Frontier, **AthenaK** shows excellent weak scaling with a parallel efficiency of 80% on up to 65536 GPUs (in this case, single GCDs). We report similar results for the Z4c and dynamical GRMHD solvers presented in Zhu et al. (2024) and Fields et al. (2024) respectively.

To test the parallel efficiency of the block-based AMR framework, we present a weak scaling test of the propagation of a linear sound wave in non-relativistic hydrodynamics. On a single device, a 128^3 root grid is decomposed into 16^3 **MeshBlocks** with one level of mesh refinement wherever the mass density is larger than the background by 50% of the wave amplitude. The wave propagates along the diagonal of the mesh, which introduces a complex pattern of refined **MeshBlocks** that must be continuously refined and de-refined as the wave propagates. On multiple devices, load balancing is required to keep the work per device roughly constant. Figure 22 shows the resulting total performance for a test run on Frontier at OLCF on up to 4096 GPUs

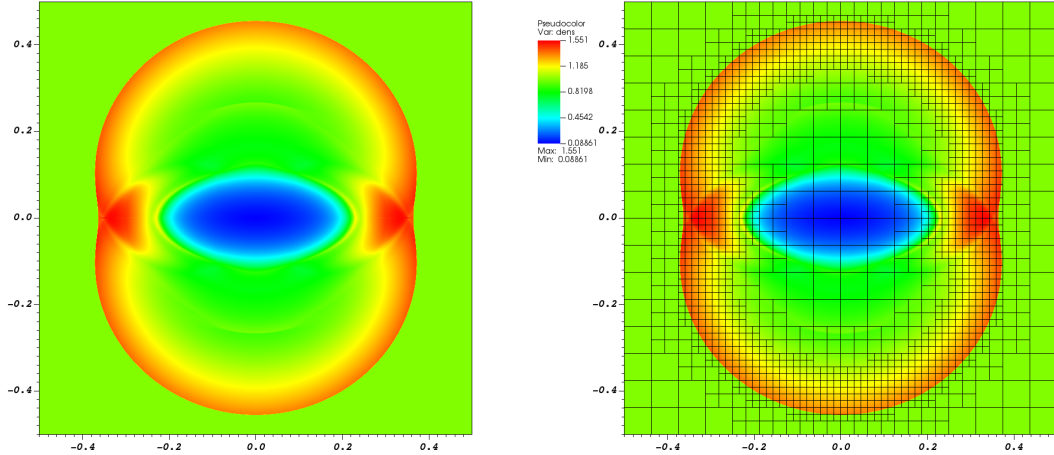


Figure 20. Density at time 0.4 in a 2D MHD blast test on a uniform (left) and AMR (right) grid run on a single NVIDIA A100 GPU. Both calculations have the same effective resolution and produce identical results, however the AMR calculation is $5.4\times$ faster.

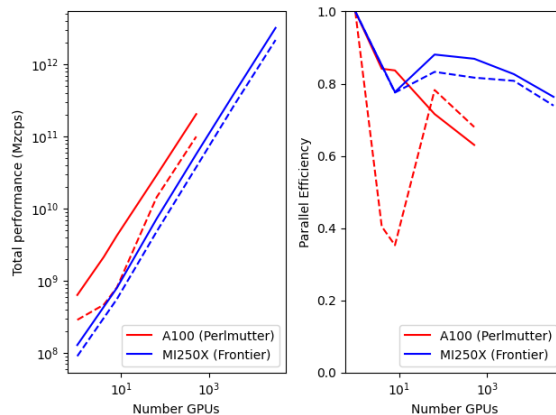


Figure 21. (Left) Total performance. (Right) Parallel efficiency.

(GCDs). Two different tests were run. The red line shows the performance as both the mesh and `MeshBlock` size is increased (the latter from 16^3 on one device to 128^3 on 512 devices, after which it is also held constant). The blue line shows the results as the `MeshBlock` size is held fixed at 32^3 above 8 GPUs. In the former case, super-linear scaling is observed, as the efficiency increases with increasing `MeshBlock` size. However, even for fixed `MeshBlock` size (blue line) nearly perfect weak scaling is observed, even though at the highest resolution over 5 million `MeshBlocks` were communicated between nodes in order to achieve good load balancing. It is clear the AMR algorithms in `AthenaK` are indeed well suited to modern HPC architectures.

6. DISCUSSION AND SUMMARY

In this paper we have described `AthenaK`, a new implementation of the `Athena++` AMR framework and various astrophysical fluid dynamic, radiation transport, and particle kinetic solvers using `Kokkos`. In two companion papers, we describe a numerical relativity solver (Zhu et al. 2024) and a GRMHD solver in dynamical spacetimes (Fields et al. 2024) based on the `AthenaK` framework. We have demonstrated that `AthenaK` achieves excellent performance and weak scaling across a wide range of architectures. On 65536 GPUs on the OLCF Frontier system, the non-relativistic hydrodynamic and MHD solvers both achieve a parallel efficiency of roughly 80%. Moreover we have shown that the block-based AMR strategy adopted by both `Athena++` and `AthenaK` is well suited for modern exascale computing systems, achieving nearly perfect weak scaling for a hydrody-

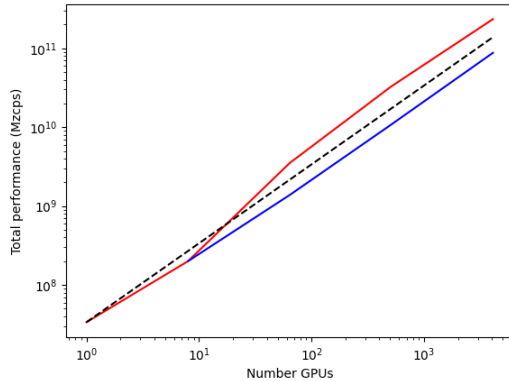


Figure 22. Total performance with AMR

namic linear wave test. The code is therefore capable of leveraging modern exascale computing systems for solving challenging problems in astrophysics.

AthenaK is a small code designed to solve specific applications at exascale. Thus, it does not implement the very broad range of algorithms and physics options that are included in **Athena++** (e.g., curvilinear coordinates). Given that it is much easier to maintain and update a smaller code, it is likely that most of the features of **Athena++** will not be implemented in **AthenaK** anytime soon. Of course, it is still possible to adopt **Athena++** or other similar codes when a particular application requires such features. Nevertheless there are several directions for future developments that are already in progress or planned for the near future. These include the addition of the fourth-order integration algorithm of [Felker & Stone \(2018\)](#), self-gravity on the AMR mesh using multigrid ([Tomida & Stone 2023](#)), and non-relativistic radiation and neutrino transport ([Jiang et al. 2012](#)).

While this paper demonstrates that the fundamental numerical algorithms adopted in **AthenaK** are well suited to the more complex design of modern HPC systems, it is nevertheless becoming increasingly challenging to develop and maintain software as part of large research projects on such systems. A significant challenge for the future will be finding the resources and expertise to develop and support increasingly complex research software. It is likely that open source frameworks such as **Kokkos** and **Parthenon** will be important in this effort.

ACKNOWLEDGMENTS

We thank Kengo Tomida for discussion regarding the AMR framework, and the many other contributors to the **Athena++** code project. We thank the members of the **Parthenon** collaboration whose input on programming with **Kokkos** was essential. We thank Matthew Cawood for providing performance numbers on NVIDIA’s Grace Hopper processor.

JS was supported by a subcontract from the Texas Advanced Computing Center from National Science Foundation grant 2139536, and by the Eric and Wendy Schmidt Funds for Strategic Innovation. ERM acknowledges partial support by the National Science Foundation under grants No. PHY- 2309210, AST-2307394, and from NASA under grant 80NSSC24K1229.

Simulations were performed on OLCF’s Frontier, ALCF’s Polaris, NERSC’s Perlmutter, and on Princeton University’s Della and Stellar supercomputers.

Many figures in this manuscript were produced with **matplotlib** ([Hunter 2007](#)), the **yt** package ([Turk et al. 2011](#)), or the **VisIt** visualization software ([Childs et al. 2012](#)).

This research used resources of the National Energy Research Scientific Computing Center, a DOE Office of Science User Facility supported by the Office of Science of the U.S. Department of Energy under Contract No. DE-AC02-05CH11231.

This research used resources of the Oak Ridge Leadership Computing Facility at the Oak Ridge National Laboratory, which is supported by the Office of Science of the U.S. Department of Energy under Contract No. DE-AC05-00OR22725.

This research used resources of the Argonne Leadership Computing Facility, a U.S. Department of Energy (DOE) Office of Science user facility at Argonne National Laboratory and is based on research supported

by the U.S. DOE Office of Science-Advanced Scientific Computing Research Program, under Contract No. DE-AC02-06CH11357.

The simulations presented in this article were partly performed on computational resources managed and supported by Princeton Research Computing, a consortium of groups including the Princeton Institute for Computational Science and Engineering (PICSciE) and

the Office of Information Technology's High Performance Computing Center and Visualization Laboratory at Princeton University.

Research presented in this article was supported by the Laboratory Directed Research and Development program of Los Alamos National Laboratory under project number 20220087DR.

This work has been assigned a document release number LA-UR-24-30139.

REFERENCES

- Acker, F., B. de R. Borges, R., & Costa, B. 2016, *Journal of Computational Physics*, 313, 726,
doi: <https://doi.org/10.1016/j.jcp.2016.01.038>
- Anninos, P., & Fragile, P. C. 2020, *ApJ*, 900, 71,
doi: [10.3847/1538-4357/abab9c](https://doi.org/10.3847/1538-4357/abab9c)
- Asahina, Y., Takahashi, H. R., & Ohsuga, K. 2020, *ApJ*, 901, 96, doi: [10.3847/1538-4357/abaf51](https://doi.org/10.3847/1538-4357/abaf51)
- Ascher, U. M., Ruuth, S. J., & Spiteri, R. J. 1997, *Applied Numerical Mathematics*, 25, 151,
doi: [https://doi.org/10.1016/S0168-9274\(97\)00056-1](https://doi.org/10.1016/S0168-9274(97)00056-1)
- Bacchini, F., Ripperda, B., Porth, O., & Sironi, L. 2019, *ApJS*, 240, 40, doi: [10.3847/1538-4365/aafcb3](https://doi.org/10.3847/1538-4365/aafcb3)
- Bai, X.-N., Caprioli, D., Sironi, L., & Spitkovsky, A. 2015, *ApJ*, 809, 55, doi: [10.1088/0004-637X/809/1/55](https://doi.org/10.1088/0004-637X/809/1/55)
- Bai, X.-N., & Stone, J. M. 2010, *ApJS*, 190, 297,
doi: [10.1088/0067-0049/190/2/297](https://doi.org/10.1088/0067-0049/190/2/297)
- Bardeen, J. M., & Petterson, J. A. 1975, *ApJL*, 195, L65,
doi: [10.1086/181711](https://doi.org/10.1086/181711)
- Beckwith, K., & Stone, J. M. 2011, *ApJS*, 193, 6,
doi: [10.1088/0067-0049/193/1/6](https://doi.org/10.1088/0067-0049/193/1/6)
- Beloborodov, A. M. 2023, *ApJ*, 959, 34,
doi: [10.3847/1538-4357/acf659](https://doi.org/10.3847/1538-4357/acf659)
- Birdsall, C., & Langdon, A. 1991, *Plasma Physics via Computer Simulation* (1st ed.) (New York: McGraw-Hill)
- Blandford, R. D., & Znajek, R. L. 1977, *MNRAS*, 179, 433,
doi: [10.1093/mnras/179.3.433](https://doi.org/10.1093/mnras/179.3.433)
- Boris, J. P. 1970, *Proceeding of Fourth Conference on Numerical Simulations of Plasmas*
- Brio, M., & Wu, C. C. 1988, *Journal of Computational Physics*, 75, 400, doi: [10.1016/0021-9991\(88\)90120-9](https://doi.org/10.1016/0021-9991(88)90120-9)
- Caddy, R. V., & Schneider, E. E. 2024, *ApJ*, 970, 44,
doi: [10.3847/1538-4357/ad464a](https://doi.org/10.3847/1538-4357/ad464a)
- Chael, A. 2024, *MNRAS*, 532, 3198,
doi: [10.1093/mnras/stae1692](https://doi.org/10.1093/mnras/stae1692)
- Chakrabarti, S. K. 1985, *ApJ*, 288, 1, doi: [10.1086/162755](https://doi.org/10.1086/162755)
- Childs, H., Brugger, E., Whitlock, B., et al. 2012, *High Performance Visualization—Enabling Extreme-Scale Scientific Insight*, doi: [10.1201/b12985](https://doi.org/10.1201/b12985)
- Colella, P. 1990, *Journal of Computational Physics*, 87, 171,
doi: [10.1016/0021-9991\(90\)90233-Q](https://doi.org/10.1016/0021-9991(90)90233-Q)
- Colella, P., & Woodward, P. R. 1984, *Journal of Computational Physics*, 54, 174,
doi: [10.1016/0021-9991\(84\)90143-8](https://doi.org/10.1016/0021-9991(84)90143-8)
- Daszuta, B., & Cook, W. 2024, *arXiv e-prints*,
arXiv:2406.05126, doi: [10.48550/arXiv.2406.05126](https://doi.org/10.48550/arXiv.2406.05126)
- Davis, S. W., & Gammie, C. F. 2020, *ApJ*, 888, 94,
doi: [10.3847/1538-4357/ab5950](https://doi.org/10.3847/1538-4357/ab5950)
- Del Zanna, L., Zanotti, O., Bucciantini, N., & Londrillo, P. 2007, *A&A*, 473, 11, doi: [10.1051/0004-6361:20077093](https://doi.org/10.1051/0004-6361:20077093)
- Evans, C. R., & Hawley, J. F. 1988, *ApJ*, 332, 659,
doi: [10.1086/166684](https://doi.org/10.1086/166684)
- Felker, K. G., & Stone, J. M. 2018, *Journal of Computational Physics*, 375, 1365,
doi: [10.1016/j.jcp.2018.08.025](https://doi.org/10.1016/j.jcp.2018.08.025)
- Fields, J., Zhu, H., Radice, D., et al. 2024, *arXiv e-prints*,
arXiv:2409.10384, doi: [10.48550/arXiv.2409.10384](https://doi.org/10.48550/arXiv.2409.10384)
- Fishbone, L. G., & Moncrief, V. 1976, *ApJ*, 207, 962,
doi: [10.1086/154565](https://doi.org/10.1086/154565)
- Florinski, V., Guo, X., Balsara, D. S., & Meyer, C. 2013, *ApJS*, 205, 19, doi: [10.1088/0067-0049/205/2/19](https://doi.org/10.1088/0067-0049/205/2/19)
- Gammie, C. F., McKinney, J. C., & Tóth, G. 2003, *ApJ*, 589, 444, doi: [10.1086/374594](https://doi.org/10.1086/374594)
- Gardiner, T. A., & Stone, J. M. 2005, *Journal of Computational Physics*, 205, 509,
doi: [10.1016/j.jcp.2004.11.016](https://doi.org/10.1016/j.jcp.2004.11.016)
- . 2008, *Journal of Computational Physics*, 227, 4123,
doi: [10.1016/j.jcp.2007.12.017](https://doi.org/10.1016/j.jcp.2007.12.017)
- Genel, S., Vogelsberger, M., Nelson, D., et al. 2013, *MNRAS*, 435, 1426, doi: [10.1093/mnras/stt1383](https://doi.org/10.1093/mnras/stt1383)
- Grete, P., Glines, F. W., & O'Shea, B. W. 2021, *IEEE Transactions on Parallel and Distributed Systems*, 32, 85,
doi: [10.1109/TPDS.2020.3010016](https://doi.org/10.1109/TPDS.2020.3010016)
- Grete, P., Dolence, J. C., Miller, J. M., et al. 2023, *The International Journal of High Performance Computing Applications*, 37, 465, doi: [10.1177/10943420221143775](https://doi.org/10.1177/10943420221143775)
- Guo, M. e. a. 2024

- Hawley, J. F., Smarr, L. L., & Wilson, J. R. 1984, *ApJ*, 277, 296, doi: [10.1086/161696](https://doi.org/10.1086/161696)
- Holmen, J. K., Grete, P., & Hernandez, O. 2024, *Concurrency Computation Practice and Experience*, 36, doi: [10.1002/cpe.8069](https://doi.org/10.1002/cpe.8069)
- Hu, Y., Xu, S., Arzamasskiy, L., Stone, J. M., & Lazarian, A. 2024, *MNRAS*, 527, 3945, doi: [10.1093/mnras/stad3493](https://doi.org/10.1093/mnras/stad3493)
- Hunter, J. D. 2007, *Computing in Science & Engineering*, 9, 90, doi: [10.1109/MCSE.2007.55](https://doi.org/10.1109/MCSE.2007.55)
- Jiang, Y.-F., Stone, J. M., & Davis, S. W. 2012, *ApJS*, 199, 14, doi: [10.1088/0067-0049/199/1/14](https://doi.org/10.1088/0067-0049/199/1/14)
- Kastaun, W., Kalinani, J. V., & Ciolfi, R. 2021, *PhRvD*, 103, 023018, doi: [10.1103/PhysRevD.103.023018](https://doi.org/10.1103/PhysRevD.103.023018)
- Kestener, P. 2017, *Ramses-GPU: Second order MUSCL-Handcock finite volume fluid solver*, *Astrophysics Source Code Library*, record ascl:1710.013
- Ketcheson, D. I. 2010, *Journal of Computational Physics*, 229, 1763, doi: [10.1016/j.jcp.2009.11.006](https://doi.org/10.1016/j.jcp.2009.11.006)
- Komissarov, S. S. 1999, *MNRAS*, 303, 343, doi: [10.1046/j.1365-8711.1999.02244.x](https://doi.org/10.1046/j.1365-8711.1999.02244.x)
- Krapp, L., Garrido-Deutelmoser, J., Benítez-Llambay, P., & Kratter, K. M. 2024, *ApJS*, 271, 7, doi: [10.3847/1538-4365/ad14f9](https://doi.org/10.3847/1538-4365/ad14f9)
- Kunz, M. W., Stone, J. M., & Bai, X.-N. 2014, *Journal of Computational Physics*, 259, 154, doi: [10.1016/j.jcp.2013.11.035](https://doi.org/10.1016/j.jcp.2013.11.035)
- Lecoanet, D., McCourt, M., Quataert, E., et al. 2016, *MNRAS*, 455, 4274, doi: [10.1093/mnras/stv2564](https://doi.org/10.1093/mnras/stv2564)
- Leismann, T., Antón, L., Aloy, M. A., et al. 2005, *A&A*, 436, 503, doi: [10.1051/0004-6361:20042520](https://doi.org/10.1051/0004-6361:20042520)
- Lemaster, M. N., & Stone, J. M. 2009, *ApJ*, 691, 1092, doi: [10.1088/0004-637X/691/2/1092](https://doi.org/10.1088/0004-637X/691/2/1092)
- Lesur, G. R. J., Baghdadi, S., Wafflard-Fernandez, G., et al. 2023, *A&A*, 677, A9, doi: [10.1051/0004-6361/202346005](https://doi.org/10.1051/0004-6361/202346005)
- Liska, M. T. P., Chatterjee, K., Issa, D., et al. 2022, *ApJS*, 263, 26, doi: [10.3847/1538-4365/ac9966](https://doi.org/10.3847/1538-4365/ac9966)
- Loureiro, N. F., Samtaney, R., Schekochihin, A. A., & Uzdensky, D. A. 2012, *Physics of Plasmas*, 19, 042303, doi: [10.1063/1.3703318](https://doi.org/10.1063/1.3703318)
- McCorquodale, P., Dorr, M., Hittinger, J., & Colella, P. 2015, *Journal of Computational Physics*, 288, 181, doi: [10.1016/j.jcp.2015.01.006](https://doi.org/10.1016/j.jcp.2015.01.006)
- Meyer, C. D., Balsara, D. S., & Aslam, T. D. 2014, *Journal of Computational Physics*, 257, 594, doi: [10.1016/j.jcp.2013.08.021](https://doi.org/10.1016/j.jcp.2013.08.021)
- Mignone, A., Zanni, C., Tzeferacos, P., et al. 2012, *ApJS*, 198, 7, doi: [10.1088/0067-0049/198/1/7](https://doi.org/10.1088/0067-0049/198/1/7)
- Most, E. R., Beloborodov, A. M., & Ripperda, B. 2024, *arXiv e-prints*, arXiv:2404.01456, doi: [10.48550/arXiv.2404.01456](https://doi.org/10.48550/arXiv.2404.01456)
- Mösta, P., Mundim, B. C., Faber, J. A., et al. 2014, *Classical and Quantum Gravity*, 31, 015005, doi: [10.1088/0264-9381/31/1/015005](https://doi.org/10.1088/0264-9381/31/1/015005)
- Olivares, H., Porth, O., Davelaar, J., et al. 2019, *A&A*, 629, A61, doi: [10.1051/0004-6361/201935559](https://doi.org/10.1051/0004-6361/201935559)
- Papaloizou, J. C. B., & Pringle, J. E. 1983, *MNRAS*, 202, 1181, doi: [10.1093/mnras/202.4.1181](https://doi.org/10.1093/mnras/202.4.1181)
- Pareschi, L., & Russo, G. 2005, *Journal of Scientific Computing*, 25, 129, doi: [10.1007/BF02728986](https://doi.org/10.1007/BF02728986)
- Porth, O., Olivares, H., Mizuno, Y., et al. 2017, *Computational Astrophysics and Cosmology*, 4, 1, doi: [10.1186/s40668-017-0020-2](https://doi.org/10.1186/s40668-017-0020-2)
- Porth, O., Chatterjee, K., Narayan, R., et al. 2019, *ApJS*, 243, 26, doi: [10.3847/1538-4365/ab29fd](https://doi.org/10.3847/1538-4365/ab29fd)
- Prather, B., Wong, G., Dhruv, V., et al. 2021, *The Journal of Open Source Software*, 6, 3336, doi: [10.21105/joss.03336](https://doi.org/10.21105/joss.03336)
- Prather, B. S. 2024, *arXiv e-prints*, arXiv:2408.01361, doi: [10.48550/arXiv.2408.01361](https://doi.org/10.48550/arXiv.2408.01361)
- Randall, D. A., Ringler, T. D., Heikes, R. P., Jones, P., & Baumgardner, J. 2002, *Computing in Science and Engineering*, 4, 32, doi: [10.1109/MCISE.2002.1032427](https://doi.org/10.1109/MCISE.2002.1032427)
- Ressler, S. M., Quataert, E., White, C. J., & Blaes, O. 2021, *MNRAS*, 504, 6076, doi: [10.1093/mnras/stab311](https://doi.org/10.1093/mnras/stab311)
- Rodriguez-Bueno, J., Dolence, J. C., Miller, J. M., Ryan, B. R., & Roberts, L. F. 2023, in *American Astronomical Society Meeting Abstracts*, Vol. 241, American Astronomical Society Meeting Abstracts, 105.47
- Schive, H.-Y., Zuhone, J. A., Goldbaum, N. J., et al. 2018, *MNRAS*, 481, 4815, doi: [10.1093/mnras/sty2586](https://doi.org/10.1093/mnras/sty2586)
- Schneider, E. E., & Robertson, B. E. 2015, *ApJS*, 217, 24, doi: [10.1088/0067-0049/217/2/24](https://doi.org/10.1088/0067-0049/217/2/24)
- . 2018, *ApJ*, 860, 135, doi: [10.3847/1538-4357/aac329](https://doi.org/10.3847/1538-4357/aac329)
- Shu, C.-W., & Osher, S. 1989, *Journal of Computational Physics*, 83, 32, doi: [10.1016/0021-9991\(89\)90222-2](https://doi.org/10.1016/0021-9991(89)90222-2)
- Sądowski, A., Narayan, R., Tchekhovskoy, A., & Zhu, Y. 2013, *MNRAS*, 429, 3533, doi: [10.1093/mnras/sts632](https://doi.org/10.1093/mnras/sts632)
- Stone, J. M., Gardiner, T. A., Teuben, P., Hawley, J. F., & Simon, J. B. 2008, *ApJS*, 178, 137, doi: [10.1086/588755](https://doi.org/10.1086/588755)
- Stone, J. M., Tomida, K., White, C. J., & Felker, K. G. 2020, *ApJS*, 249, 4, doi: [10.3847/1538-4365/ab929b](https://doi.org/10.3847/1538-4365/ab929b)
- Tomida, K., & Stone, J. M. 2023, *ApJS*, 266, 7, doi: [10.3847/1538-4365/acc2c0](https://doi.org/10.3847/1538-4365/acc2c0)
- Toro, E. F. 2013, *Riemann solvers and numerical methods for fluid dynamics: a practical introduction* (Springer Science & Business Media)

- Trott, C. R., Lebrun-Grandié, D., Arndt, D., et al. 2022, IEEE Transactions on Parallel and Distributed Systems, 33, 805, doi: [10.1109/TPDS.2021.3097283](https://doi.org/10.1109/TPDS.2021.3097283)
- Turk, M. J., Smith, B. D., Oishi, J. S., et al. 2011, The Astrophysical Journal Supplement Series, 192, 9, doi: [10.1088/0067-0049/192/1/9](https://doi.org/10.1088/0067-0049/192/1/9)
- Uzdensky, D., Loureiro, N., & Schekochihin, A. 2010, PhRvL, 105, 235002
- Vanthieghem, A., & Levinson, A. 2024, arXiv e-prints, arXiv:2407.15076, doi: [10.48550/arXiv.2407.15076](https://doi.org/10.48550/arXiv.2407.15076)
- Visser, M. 2007, arXiv e-prints, arXiv:0706.0622, doi: [10.48550/arXiv.0706.0622](https://doi.org/10.48550/arXiv.0706.0622)
- Wang, N., & Lee, J.-L. 2011, SIAM Journal on Scientific Computing, 33, 2536, doi: [10.1137/090761355](https://doi.org/10.1137/090761355)
- White, C. J., Mullen, P. D., Jiang, Y.-F., et al. 2023, ApJ, 949, 103, doi: [10.3847/1538-4357/acc8cf](https://doi.org/10.3847/1538-4357/acc8cf)
- White, C. J., Stone, J. M., & Gammie, C. F. 2016, The Astrophysical Journal Supplement Series, 225, 22, doi: [10.3847/0067-0049/225/2/22](https://doi.org/10.3847/0067-0049/225/2/22)
- Zhang, W., Almgren, A., Beckner, V., et al. 2019, The Journal of Open Source Software, 4, 1370, doi: [10.21105/joss.01370](https://doi.org/10.21105/joss.01370)
- Zhu, H., Fields, J., Zappa, F., et al. 2024, arXiv e-prints, arXiv:2409.10383, doi: [10.48550/arXiv.2409.10383](https://doi.org/10.48550/arXiv.2409.10383)